Altered oligodendroglia and astroglia in chronic traumatic encephalopathy

K. Blake Chancellor[1,7,*], Sarah E. Chancellor[2,7], Joseph E. Duke-Cohan[1], Bertrand R. Huber[2-4,6], Thor D. Stein[2,4,5,6], Victor E. Alvarez[2-4,6], Ann C. McKee[2-6,*]

[1]Department of Genetics, Harvard Medical School, Boston, MA, USA. [2]Alzheimer's Disease and Chronic Traumatic Encephalopathy Center, Boston University School of Medicine, Boston, MA, USA. [3]Department of Neurology, Boston University School of Medicine, Boston, MA, USA. [4]Department of Pathology and Laboratory Medicine, VA Boston Healthcare System, Boston, MA, USA. [5]Department of Pathology, Boston University School of Medicine, Boston, MA, USA. [6]Edith Nourse Rogers VA Medical Center. [7]These authors contributed equally to this work. *Corresponding author.

* Correspondence should be addressed to K.B.C. (chancellor@g.harvard.edu) and A.C.M. (amckee@bu.edu)

Abstract

Chronic traumatic encephalopathy (CTE) is a progressive tauopathy found in contact sport athletes, military veterans, and others exposed to repetitive head injury (McKee et al. 2009, 2013, 2016; Omalu et al. 2005, 2006; Martland 1928; Critchley 1949). White matter atrophy and axonal loss have been reported in CTE but have not been characterized on a molecular or cellular level (McKee et al. 2013; Holleran et al. 2017; Hsu et al. 2018). Here, we report 24,735 single nucleus RNA-seq profiles from dorsolateral frontal white matter cell nuclei from eight individuals with neuropathologically confirmed CTE and eight age- and sex-matched controls. We identified eighteen transcriptionally distinct nuclei clusters, as well as cell-type-specific differences between conditions. The findings support a global loss of oligodendrocytes (OLs) in CTE, alterations in OL subpopulations, and suggest pathological iron accumulation in OL subpopulations. Total astrocyte number was not different between CTE and controls but showed upregulation of transcripts associated with neuroinflammation. These findings provide novel insight into the molecular and cellular underpinnings of white matter atrophy in CTE, which may lead to an improved understanding of the disease pathogenesis.

Introduction

Chronic traumatic encephalopathy (CTE) is a progressive tauopathy associated with exposure to repetitive head injury (RHI) (McKee et al. 2009, 2013, 2016; Omalu et al. 2005, 2006; Martland 1928; Critchley 1949). CTE has been reported in contact sport athletes, veterans exposed to blast and other mild traumatic brain injuries, and victims of domestic abuse (McKee et al. 2009, 2013). The symptoms of CTE include impulsivity, explosivity, depression, memory impairment, and executive dysfunction (Stern et al. 2013; Montenigro et al. 2014; McKee et al. 2013; Mez et al. 2017); however, like most neurodegenerative diseases, a definitive diagnosis of CTE requires postmortem neuropathologic examination. A National Institute of Neurological Disease and Stroke (NINDS)/National Institute of Biomedical Imaging and Bioengineering (NIBIB) panel defined the pathognomonic lesion of CTE as the perivascular accumulation of hyperphosphorylated tau (p-tau) in neurons and astrocytes in an irregular pattern in the cerebral cortex, most prominent at the depths of the sulci (McKee et al. 2016). The distinctive p-tau pathology of CTE primarily involves gray matter structures of the frontal, parietal and temporal cortex, medial temporal lobe, diencephalon and brainstem (McKee et al. 2013). However, white matter atrophy, white matter rarefaction, myelin and axonal loss, astrocytic degeneration, and p-tau pathology in the cortical white matter have also been described (McKee et al. 2013; Holleran et al. 2017; Hsu et al. 2018). Furthermore, white matter rarefaction is independently associated with dementia in CTE in addition to p-tau pathology and inflammation (Alosco et al. 2019; Cherry et al. 2016).

High-throughput single cell resolution genomics is an ideal tool for assessing the complexity of human brain diseases (Mathys et al. 2019; Jäkel et al. 2019; Velmeshev et al. 2019; Schirmer et al. 2019; Grubman et al. 2019; Nagy et al. 2020). To better understand the pathobiology of white matter alterations in CTE, we performed a single nucleus RNA-seq (Habib et al. 2017) (snRNA-seq) analysis of dorsolateral frontal white matter in subjects with neuropathologically confirmed CTE and compared the results to age-matched controls. Our analysis yielded 24,735 brain nuclei profiles and provide a resource to better understand the complex cellular interactions and gene expression profiles that may contribute to the pathogenesis of CTE. Similar to previous reports using snRNA-seq in other neurological diseases, including Alzheimer's disease (AD), multiple sclerosis (MS), autism spectrum disorder (ASD), and epilepsy (Mathys et al. 2019; Grubman et al. 2019; Jäkel et al. 2019; Schirmer et al. 2019; Velmeshev et al. 2019), our findings indicate changes in cell types, subpopulations, and gene expression in CTE. Our findings are the first report of molecular and cellular changes at single nucleus resolution in CTE.

Results

Single nucleus RNA-seq profiling of human CTE white matter

We collected fresh-frozen white matter tissue from the dorsolateral frontal cortex (Brodmann area 8/9) from 16 age- and post-mortem interval (PMI)-matched male individuals from the Veterans Affairs-Boston University-Concussion Legacy Foundation (VA-BU-CLF)/ Understanding Neurological Injury and Traumatic Encephalopathy (UNITE) Brain Bank and the National Posttraumatic Stress Disorder (PTSD) Brain Bank (Fig. 1a, Supplementary Fig. 1a,b,c,d). Clinical demographics, cause of death, neuropathological diagnoses, and history of RHI are provided in

Supplemental Table 1. Brain tissue was collected from 8 individuals neuropathologically diagnosed with CTE stage II or III (McKee et al. 2013, 2016) and 8 individuals with no neuropathological evidence of disease and no history of RHI. All 8 CTE subjects were former collegiate or professional American football players (Supplementary Table 1). Brodmann Area 8/9 was selected as it is an area of early and severe p-tau pathology in CTE and has been previously found to have axonal microstructural changes in CTE (Holleran et al. 2017). Moreover, pathology in Brodmann area 8/9 might underlie some of the disabling symptoms of CTE, including depression, impulsivity, memory deficits, and impaired executive function (Koenigs and Grafman 2009; Sala et al. 2011; Funahashi and Andreau 2013; Barbey, Colom, and Grafman 2013; Mahar, Alosco, and McKee 2017). Subjects with CTE stage II and III were selected in order to reveal potential key molecular events at a moderate stage of the disease when most subjects are overtly symptomatic yet are not end-stage. All subjects with CTE had no other co-morbid neurodegenerative disease, such as AD, Lewy body disease or frontotemporal lobar degeneration.

Previous transcriptomic analysis in CTE has been limited by the nature of bulk tissue analysis, which obscures important cell-type-specific changes that may be critical to disease progression (Seo et al. 2017). Here, we performed the first snRNA-seq analysis of CTE. We report a total of 24,735 droplet-based snRNA-seq profiles across 16 subjects with a median of 549 genes and 832 unique molecular identifiers (UMIs) per nucleus (Supplementary Fig. 1e,f,g).

Cellular diversity and cell-type-specific changes in CTE white matter

For snRNA-seq analysis, we isolated tissue from 1cm^3 frozen tissue blocks of Brodmann area 8/9. We isolated the white matter immediately beneath the cortical ribbon at the depth of the sulcus in order to target the subcortical U-fibers, a population in which pathological abnormalities have been observed in CTE (McKee et al. 2009) and axonal microstructural alterations have been found on post-mortem diffusion tensor imaging (Holleran et al. 2017) (Fig. 1a, Supplementary Fig. 1a). For in situ validations, we collected frozen tissue sections from Brodmann area 8/9 containing both cortical and white matter tissue from the area directly adjacent to the block taken for snRNA-seq analysis (Supplementary Fig. 1a).

From isolated tissue blocks, we extracted intact nuclei for inDrops single nucleus encapsulation and sample preparation (Klein et al. 2015; Zilionis et al. 2017). Following sequencing, we performed downstream computational analysis using the Seurat analysis pipeline (Butler et al. 2018; Hafemeister and Satija 2019) to produce single nucleus transcriptomic profiles of 16 control and CTE subjects (Fig. 1a,b). Using the Seurat analysis pipeline, we performed a variety of quality control measures to identify high-quality nuclei for further analysis. This process included filtering nuclei with fewer than 400 genes and more than 2,500 genes. We also removed nuclei with more than 1% mitochondrial genes. To identify cell-types in our data set, we constructed an unbiased *k*-nearest neighbor graph based on top principal components followed by a Jaccard similarity step and the Louvain modularity optimization algorithm (Blondel et al. 2008) to group our cell nuclei by gene expression similarities and produce a two-dimensional t-distributed stochastic neighbor embedding (tSNE) projection (Butler et al. 2018; Maaten and Hinton 2008). While the underlying tSNE algorithm performs an unbiased analysis to group nuclei by gene expression similarities, each tSNE produced is highly dependent on the parameters selected prior to analysis (i.e., number of principal components, number of highly variable genes, resolution) (Kobak and Berens 2019).

To produce a robust tSNE for further analysis, we fine-tuned parameters over various iterations to identify clusters that appeared consistently (Kobak and Berens 2019; Jäkel et al. 2019; Mathys et al. 2019; Grubman et al. 2019; Schirmer et al. 2019; Velmeshev et al. 2019). After comparing a variety of parameters, we chose 23 principal components and a resolution of 0.8 for input parameters (Supplementary Fig. 1h), and we identified an integrated tSNE projection with 18 transcriptionally distinct nuclei clusters derived from control and CTE samples (Fig. 1b, left). When we separated our tSNE by condition, we observed several clusters that appeared to be specific to one condition (Fig. 1b, middle). To identify which cell-types were perturbed, we labeled clusters of nuclei by expression of canonical cell-type marker genes: *PLP1* for oligodendrocytes (OLs), *GFAP* for astrocytes, *VCAN* for oligodendrocyte precursor cells (OPCs), *CD74* for microglia, *NRGN* for excitatory neurons, *GAD1* for interneurons, and *CLDN5* for endothelial cells (Mathys et al. 2019; Jäkel et al. 2019; Grubman et al. 2019; Velmeshev et al. 2019; Schirmer et al. 2019) (Fig. 1c, Supplementary Fig. 2). Combining control and CTE subjects, we identified a total of 18,491 oligodendrocytes (~75%), 2,598 astrocytes (~11%), 1,879 OPCs (~8%), 596 microglia (~2%), 857 excitatory neurons (~3%), 271 interneurons (~1%), and 43 endothelial cells (~0.2%).

Upon generation of our final tSNE projection labeled by cell-type marker genes, we identified an apparent global depletion of OLs, a potential increase in OL subpopulations, and a shift in astrocyte subpopulations in CTE. To determine whether observed differences between conditions were the result of subject-specific variation, with a single subject from a cohort having fewer OLs and another having an increase in an OL subpopulation, thus obscuring the actual underlying biological processes at play, we normalized nuclei numbers (see methods in (Schirmer et al. 2019)) and compared the distributions of total nuclei in each cluster by subject (Fig. 1d). While we did observe subject-specific variation in our data, we were able to identify significant differences between conditions. Specifically, we observed a subpopulation of OLs that was significantly increased across all 8 CTE subjects, suggesting a potential OL disease state (Jäkel et al. 2019; Falcão et al. 2018). Bulk gene expression comparison between conditions additionally revealed several genes previously implicated in neurodegeneration. We identified an upregulation of *DPP10* (encodes a voltage-gated potassium channel protein positively associated with p-tau-positive neurofibrillary tangles (Chen, Gai, and Abbott 2014)), an upregulation of *CLU* (encodes a glycoprotein positively associated with Aß toxicity and cell stress (Foster et al. 2019)), an upregulation of *DTNA* (encodes an astrocytic protein associated with dementia status and p-tau aggregation (Simon et al. 2018)), and a downregulation of *RNF220* (an untranslated variant associated with cholesterol metabolism and neurodegeneration (Akila Parvathy Dharshini, Taguchi, and Michael Gromiha 2019)) (Fig. 1e). Of particular note, we identified a downregulation *FA2H* (Kruer et al. 2010) and *TF* (Mariani et al. 2013), two genes associated with iron accumulation and Neurodegeneration with Brain Iron Accumulation (NBIA) (Fig. 1e).

Global depletion of OLs in CTE white matter

To further investigate the cell-type-specific changes associated with OLs in CTE, we isolated OL nuclei clusters from our primary tSNE projection and re-projected OL nuclei as a subset tSNE (Kobak and Berens 2019; Grubman et al. 2019) (Fig. 2a). To do this, we first identified each nucleus that was previously identified as an OL. We subset the OL nuclei and performed the unbiased graph-based clustering steps described above to produce an OL-specific tSNE. This approach allows for a higher resolution comparison between conditions by removing all non-OL

cell-types and focusing the comparison on OLs. Consistent with our primary tSNE projection, we observed an apparent global loss of OLs in CTE and the presence of CTE-specific OL subpopulations. To address whether these differences were driven by a subset of subjects, we compared normalized nuclei counts between conditions (Fig. 2b, Methods). We observed a significant decrease in the number of OLs across all 8 CTE subjects (FDR-corrected $P = 0.01$, Mann-Whitney U test). These findings suggest potential OL cell death and myelin loss, similar to what has been observed in MS lesions (Jäkel et al. 2019).

Using tissue blocks adjacent to the region used in our snRNA-seq analysis, we next performed immunohistochemistry (IHC) and RNA in situ hybridization to assess whether we could also observe global loss of OLs in situ (Fig. 2c,d, Supplementary Fig. 3). By IHC, we observed a depletion of OLs consistent with our snRNA-seq findings ($P = 0.04$, one-tailed Student's t-test) (Fig. 2c, Supplementary Fig. 3a,b), and by RNA in situ hybridization, we further confirmed our findings ($P = 0.02$, one-tailed Student's t-test) (Fig. 2d, Supplementary Fig. 3c,d). Furthermore, using IHC, the loss of OLs was not restricted to the subcortical U-fibers but was detected throughout the entire subcortical white matter sample for each subject (Fig. 2c, Supplementary Fig. 3a,b). The in situ probes used in these analyses also identify OPCs, however, we did not observe differences in OPC numbers in our snRNA-seq analysis ($P = 0.13$, Mann-Whitney U test) (Supplementary Fig. 4a,b). To verify that our in situ validation results were not driven by changes in OPC numbers, we performed IHC analysis to detect changes in the total number of OPCs between conditions (Supplementary Fig. 4c). We did not observe a difference in the total number of OPCs between control and CTE subjects suggesting that the OL loss was specific to mature OLs ($P = 0.23$, one-tailed Student's t-test).

To further understand the gene expression changes that might be driving the observed OL differences in CTE, we tested for differential gene expression between conditions. The most differentially expressed genes between conditions included *CRYAB* (anti-apoptotic and neuroprotective factor (Zhang et al. 2019; Ousman et al. 2007; Schirmer et al. 2019)) and *FTH1* (iron accumulation (Iancu 1992; Vidal et al. 2004; Schirmer et al. 2019)) (Fig. 2e).

Taken together, these analyses demonstrate a loss of OLs in CTE supporting OL death and myelin loss, and a potential role for iron accumulation and apoptosis as contributing factors in CTE pathogenesis.

Iron accumulation and cell stress in CTE-specific OLs

After observing shifts in OL subpopulations in CTE, we wondered whether these shifts were specifically related to disease pathogenesis. We first considered the global loss of OLs in CTE in contrast with the apparent emergence of CTE-specific OL subpopulations (Fig. 3a). To determine whether these CTE-specific subpopulations were consistently increased across all CTE subjects, we compared normalized nuclei counts between conditions (Fig. 3b, Methods). All 3 CTE-specific OL groups (OL6, OL7, and OL8) were significantly increased across all subjects in CTE. We used cell-type marker analysis to identify the most upregulated genes in these clusters and found that these clusters are likely driving the upregulation of iron accumulation and cell stress genes observed in the differential gene expression test described above. Gene expression analysis between conditions once again revealed an increase in iron accumulation genes (*FTH1* and *FTL*

(Iancu 1992; Vidal et al. 2004)) and a cell stress gene (*CRYAB* (Ousman et al. 2007; Zhang et al. 2019)) (Fig. 3c). While we did observe an increase of three separate OL subpopulations in CTE, further gene expression analysis allowed us to identify OL6 as the primary subpopulation responsible for the upregulation of iron accumulation genes (Fig. 3d).

To further investigate whether iron accumulation is dysfunctional in CTE, we performed an in situ analysis to detect the presence of iron aggregates (hemosiderin) (Rowatt et al. 2018; Iancu 1992) (Fig. 3e, Supplementary Fig. 5a). Consistent with our snRNA-seq findings, we observed an increase in the total number of iron inclusions in CTE tissue compared to control ($P = 0.04$, one-tailed Student's t-test), which may support the hypothesis that aberrant iron accumulation is a contributing factor to the pathogenesis of CTE.

Finally, to validate the presence of OLs with upregulated *FTH1* and *CRYAB*, we performed RNA in situ hybridization on control and CTE subjects (Fig. 3f, Supplementary Fig. 5c). Consistent with the snRNA-seq and in situ analyses revealing reduced numbers of OLs in CTE, clusters of *OLIG2* positive nuclei were sparse by RNA in situ hybridization. When groups of *OLIG2* positive nuclei were found, RNA in situ hybridization revealed the presence of cell clusters with gene expression profiles consistent with the OL6 subpopulation observed in our data. These analyses support the hypothesis that OLs in CTE are involved in toxic iron accumulation with resultant cell stress and OL death.

No changes in astrocyte cell number in CTE white matter

We next looked for other cell-type-specific changes associated with CTE and identified a potential change in the expected heterogeneity of astrocytes (Supplementary Fig. 6a). In many neurological diseases, the total number of astrocytes is increased and highly motile "reactive" astrocytes predominate (Clarke et al. 2018; Liddelow et al. 2017; Liddelow and Barres 2017; Schirmer et al. 2019). We compared the total number of astrocytes between conditions and did not see a difference in the total number of astrocytes in CTE (McKee et al. 2013) ($P = 0.29$, Mann-Whitney U test) (Supplementary Fig. 6b). We confirmed this finding by IHC and RNA in situ hybridization ($P = 0.44$ and $P = 0.50$, respectively; one-tailed Mann Whitney U-test) (Supplementary Fig. 6c,d).

Identification of neuroinflammatory astrocytes in CTE white matter

To interrogate the emergence of astrocyte subpopulations in CTE, we isolated all astrocytes from our primary tSNE and re-projected each astrocyte nucleus as a subset tSNE, similar to the analysis described above for OLs (Fig. 4a). We observed the emergence of two CTE-specific astrocyte subpopulations: Astrocyte2 and Astrocyte3 (Fig. 4a). We compared normalized nuclei numbers between conditions (Fig. 4b, Methods) and found a significant decrease in Astrocyte1 and a significant increase in Astrocyte2 and Astrocyte3 in CTE. We performed cell-type marker analysis to reveal the genes driving each subpopulation. Astrocyte1 expressed many genes associated with normal functioning astrocytes (e.g. *GFAP, CTNND2, AQP4*), Astrocyte2 expressed genes associated with dysfunctional metabolism (e.g. *PDK4* (Jha, Jeon, and Suk 2012)), and Astrocyte3 expressed genes associated with neuroinflammation and aging (*CD44*, *BCL6*, and *SERPINA3* (Liddelow et al. 2017; Schirmer et al. 2019)). Further analysis of Astrocyte3 gene expression again revealed an increase in neuroinflammatory genes (Fig. 4c). Examining the expression of these

neuroinflammatory genes on our astrocyte-specific tSNE further supported the finding that Astrocyte3 represents an astrocyte subpopulation involved in neuroinflammation (Fig. 4d).

To validate the presence of astrocytes with upregulated *CD44*, we performed double-labeled immunofluorescence staining which identified CD44-positive, GFAP-positive astrocytes in CTE (Fig. 4e, Supplementary Fig. 7a). We observed a significant increase in CD44-expression in CTE tissue by immunofluorescence ($P = 0.02$, one-tailed Student's t-test) (Fig. 4e, right). By RNA in situ hybridization we identified astrocytes with upregulated *CD44* and *BCL6* (Fig. 4f, Supplementary Fig. 7b), and quantification of *BCL6* transcripts revealed a potential increase in total *BCL6* expression in CTE tissue ($P = 0.06$, one-tailed Student's t-test) (Fig. 4f, right).

Using gene expression and in situ analyses, we were able to identify astrocyte subpopulations with transcriptional profiles similar to those often observed in neuroinflammatory astrocytes (Liddelow and Barres 2017). However, we wondered whether CTE-specific astrocytes were perturbed in a more general sense. To address this, we performed gene ontology (GO) analysis using differentially expressed genes in CTE-specific astrocytes to identify biological processes significantly enriched in CTE-specific astrocytes. GO analysis revealed a significant increase of processes often associated with disease-associated astrocytes such as protein folding, heat response, and regulation of apoptosis (Fig. 4g).

Together, these analyses demonstrate that the total number of astrocytes in CTE is not changed but there is an increase in subpopulations of astrocytes involved in neuroinflammation and dysfunctional metabolic states. These findings support the possibility that astrocytes in CTE do not recruit additional astrocytes, but instead, alter their genetic profiles to become neuroinflammatory in a challenged environment.

Discussion

We performed the first snRNA-seq transcriptomic analysis of the white matter in CTE, a progressive neurodegenerative disease associated with an array of behavioral, mood, and cognitive symptoms that often progress to dementia (McKee et al. 2013, 2016; Stern et al. 2013; Mez et al. 2017). We report a total of 24,735 nuclei across 16 male subjects, 8 with neuropathologically verified CTE and 8 age- and PMI-matched controls. The pathognomonic lesion of CTE is a perivascular collection of p-tau aggregates in neurons and astroglia that occurs in the cortical gray matter, often at the depth of the dorsolateral frontal sulcus (McKee et al. 2013, 2016), that is associated with white matter rarefaction, myelin and axonal loss, and astrocytic degeneration in the frontal white matter (McKee et al. 2013, 2015; Holleran et al. 2017; Tagge et al. 2018). By performing snRNA-seq in the white matter at the depth of the dorsolateral frontal sulcus, our study identified a loss of oligodendroglia in CTE accompanied by alterations in oligodendroglial and astrocyte subpopulations. OL loss in CTE occurred in contrast with the emergence of 3 OL subpopulations, each expressing genes associated with cell stress and iron accumulation (*CRYAB* (Ousman et al. 2007) and *FTH1* (Iancu 1992; Vidal et al. 2004)). In addition, although we did not find a change in overall astrocyte number, we observed an increase in astrocytic subpopulations involved in neuroinflammation and dysfunctional metabolism.

This study is the first of its kind to examine the molecular and cellular changes in CTE using snRNA-seq transcriptomic analysis and the first to specifically focus on alterations in the white matter in CTE. A unifying hypothesis in the pathogenesis of CTE is that RHI, including multiple concussions and subconcussive impacts, produces multifocal injury to the axons and small blood vessels of the brain, with resultant blood brain barrier dysfunction and persistent neuroinflammation. This hypothesis is supported by human pathological studies of acute concussive injury that show multifocal traumatic axonal injury, microglial activation, and microhemorrhage with accumulation of macrophages containing hemosiderin, a major iron storage protein, in the brain (Blumbergs et al. 1994; Oppenheimer 1968; McKee et al. 2014; Tagge et al. 2018). Furthermore, in some young individuals after RHI, perivascular hemosiderin-laden macrophages are associated with focal deposition of p-tau (McKee et al. 2014; Tagge et al. 2018), suggesting that microvascular damage and breach of the blood brain barrier is mechanistically linked to the development of p-tau pathology. Neuroinflammation, blood brain barrier leakage and hemosiderin-laden macrophages are also key features of CTE (Cherry et al. 2016; Doherty et al. 2016; McKee et al. 2016). Magnetic resonance imaging (MRI) has shown that iron deposits are present in multiple cortical and white matter locations after RHI and are associated with cognitive impairment (Raz et al. 2011; Nisenbaum, Novikov, and Lui 2014; Lu et al. 2015). Iron accumulation induces transcription of ferritin (*FTH1* and *FTL*) (Munro 1990) and also activates ferroptosis, a form of regulated cell death characterized by the iron-dependent accumulation of lipid hydroperoxides (Stockwell et al. 2017). Taken together, our results support a potential role for OLs in the pathogenesis of CTE through accumulation and storage of excess iron, transcription of ferritin (*FTH1* and *FTL*), upregulation of anti-apoptotic genes (*CRYAB*), and OL cell death.

Combining transcriptomic analysis with in situ validation, we were able to identify salient findings that persisted across experimental methods. However, this work is limited by a couple of technical factors. First, we were limited by available human subjects who fit our experimental criteria, thus resulting in a modest sample size. Second, we used the inDrops single cell method, rather than the 10X Genomics single cell method. While we were able to achieve sufficient data quality to identify interpretable results, using a more recent single cell method may have resulted in more genes and UMIs per nucleus. Regardless, these data provide a valuable resource for understanding the molecular and cellular changes associated with CTE pathogenesis, and this data set can be easily integrated with future data sets to build a more comprehensive single cell transcriptomic profile of CTE.

Overall, our findings contribute to our understanding of the molecular and cellular changes associated with CTE pathogenesis; however, it remains to be determined whether similar changes also occur within the frontal gray matter in CTE as well as in other regions of the brain. It will also be important to ascertain whether these findings are present after RHI either prior to or in the earliest stage of CTE (stage I) and if they change in parallel with the progression of p-tau pathological severity in CTE. Correlating these changes with symptom severity and performing single cell transcriptomics in other brain regions is a focus of future work. To add to our findings, future work could also include investigating the mechanism by which toxic iron accumulation leads to OL cell death, as well as the role of neuroinflammatory astrocytes in disease progression. Overall, understanding the role of various cell populations in the pathogenesis of CTE will likely be important for targeting therapies and developing biomarkers for in life disease diagnosis.

Methods

Human patient selection

CTE subjects were selected based on a neuropathologically verified diagnosis of CTE stage II or stage III by A.C.M., T.D.S., B.R.H. or V.E.A. without any co-morbid neurodegenerative disease and availability of fresh frozen from dorsolateral frontal cortex (Brodmann area 8/9), Control subjects were age-, PMI-, RIN-, and sex-matched (all males) with neuropathological confirmation of the absence of neurological or neurodegenerative disease and availability of fresh frozen tissue from dorsolateral frontal cortex (Brodmann area 8/9). For the snRNA-seq analysis, the subcortical white matter was dissected from the tissue blocks and included both U-fibers and deep white matter. For the in situ analysis, a section of Brodmann area 8/9 tissue with both cortical and white matter tissue adjacent to the white matter block taken for snRNA-seq analysis was isolated. Subject ages were not significantly different (Control: 55.6 ± 7.5 years; CTE: 55.9 ± 10.7 years; $P = 0.90$, Mann-Whitney U test). Subject PMI was not significantly different (Control: 31.7 ± 9.7 hours; CTE: 35.3 ± 10.2 hours; $P = 0.25$, Mann-Whitney U test). Subject RIN values were not significantly different (Control: 6.4 ± 1.7; CTE: 6.8 ± 1.7; $P = 0.72$, two-tailed Student's t-test). RIN number determination was completed according to manufacturer instructions using a Bioanalyzer RNA 6000 Nano kit (Agilent).

Isolation of nuclei from frozen post-mortem human brain tissue

All tissue was macrodissected into 30mg sections from dorsolateral frontal white matter (Brodmann area 8/9) with a scalpel blade and stored at -80C. On the day of single nucleus encapsulation, tissue was placed in a 7mL dounce with ice cold buffer (0.5M sucrose, 2M KCl, 1M MgCl2, 1M Tricine-KOH pH 7.8, spermine, spermidine, DTT, RNasin, H2O) and dounced with a tight pestle ten times to mechanically dissociate and homogenize the tissue. To further dissociate the tissue, 5% IGEPAL-CA630 was added to the homogenate and dounced 5 times. The homogenate was then strained through a 40µm cell strainer (VWR) on ice. 5mL of 50% iodixanol was added to the homogenate and mixed. In a 13mL ultraclear ultracentrifuge tube, 1mL of 40% iodixanol was added with 1mL of 30% iodixanol carefully layered on top, followed by 10mL of the tissue homogenate. The tissue was then ultracentrifuged in a swing-bucket rotor at 10,000xg for 18 minutes. Following ultracentrifugation, the 35% iodixanol layer was collected and the nuclei were counted. Nuclei were diluted with 30% iodixanol to 90,000 nuclei/mL for inDrops chip loading. Nuclei were isolated for inDrops using a previously described method (Hrvatin et al. 2018).

Droplet-based snRNA-seq with inDrops and sequencing

Isolated nuclei were delivered to the inDrops single cell core facility at Harvard Medical School. The inDrops core facility produced 9,000 inDrops V3 nuclei libraries per subject by encapsulating each nucleus in a hydrogel containing barcodes and unique molecular identifiers (UMIs). Nuclei were lysed and each free mRNA molecule was reverse transcribed and labeled with a barcode and UMI, producing labeled cDNA molecules for all 16 samples. Sample cDNA was delivered to the Biopolymers Facility at Harvard Medical School. Sample quality was assessed by Agilent

Tapestation. Samples with excess primer dimer contamination were filtered by SPRIselect size selection (Beckman Coulter, B23317), followed by pooling of libraries and dilution for sequencing. Pooled samples were sequenced on the Illumina NextSeq500 at an average of 40,000 reads per nucleus barcode, approximately 360,000,000 reads per sample.

Pre-processing snRNA-seq sequencing data

The Biopolymers Core Facility delivered Binary Base Call (BCL) files for each sequencing run. The inDrops single cell method requires four primers to completely capture and de-multiplex a cDNA molecule. The first primer captures the transcript, the second captures part of the single cell barcode, the third captures the library or sample index, and the fourth captures the rest of the single cell barcode, the UMI, and the polyT tail. BCL files produced by sequencing were converted to 4 FastQ files, one per inDrops primer read. FastQ files were de-multiplexed by first filtering reads, only keeping reads that followed the expected inDrops index structure, described above. Reads that passed structure filtering were de-multiplexed based on library index, resulting in reads by sample of origin, i.e., subject. Abundant barcodes were identified and sorted so that each cDNA from a single nucleus was grouped together. During sample preparation, every cDNA molecule was labeled with a unique molecular identifier (UMI), which avoids any single molecule being counted more than once due to PCR amplification. After each read was de-multiplexed, thus assigning reads to nucleus of origin and nuclei to sample of origin, reads were aligned with bowtie/1.1.1 to an edited version of the GRCh38.97 reference genome so that all exonic and intronic reads were counted. Aligned reads were quantified and a UMI count matrix was produced for each sample. De-multiplexing was executed following the inDrops analysis pipeline (https://github.com/indrops/indrops).

Quality control and cell filtering

UMI count matrices for each subject were loaded into R version 3.6.1 using the Scater R package (McCarthy et al. 2017). Control samples were combined and CTE samples were combined to generate two separate objects with the R package Seurat version 3.1 (Butler et al. 2018). Seurat objects were filtered to exclude any nuclei with fewer than 400 genes, more than 2,
500 genes, and more than 1% mitochondrial genes. The 2 objects were then normalized and log-transformed using Seurat's implementation of SCTransform and integrated using Seurat's implementation of canonical correlation analysis (Hafemeister and Satija 2019; Butler et al. 2018) (CCA). Integration was performed to integrate control and CTE samples, thus creating a single Seurat object for downstream analyses, "CTE.combined."

Cell clustering

The single integrated Seurat object, "CTE.combined," was scaled using ScaleData and a principal component analysis (PCA) was performed for initial dimensionality reduction. An Elbow Plot was produced to determine the number of principal components to be used for further analyses (Supplementary Fig. 1h). Based on the Elbow Plot, 23 principal components were used. Using RunTSNE, FindNeighbors, and FindClusters, "CTE.combined" was further reduced in dimensionality to produce a two-dimensional t-distributed stochastic neighbor embedding (tSNE) projection. This process included constructing an unbiased *k*-nearest neighbor graph based on top

principal components followed by a Jaccard similarity step and the Louvain modularity optimization algorithm. Parameters, including resolution, were varied over several iterations to identify a tSNE that was in agreement with published human brain data and that represented nuclei clusters that were consistently present over several iterations. The final tSNE projection used was produced at resolution 0.8 and included 18 transcriptionally distinct nuclei clusters.

Cell-type annotation and sub-clustering

Nuclei clusters were annotated using canonical cell-type marker genes: *PLP1* for oligodendrocytes, *GFAP* for astrocytes, *VCAN* for oligodendrocyte precursor cells, *CD74* for microglia, *NRGN* for excitatory neurons, *GAD1* for interneurons, and *CLDN5* for endothelial cells. FindAllMarkers and FindMarkers were used to identify cluster-specific genes (Mathys et al. 2019; Schirmer et al. 2019; Jäkel et al. 2019; Grubman et al. 2019). Top genes for each cluster and the expression of top genes on the tSNE were used to identify clusters (Fig. 1c, Supplementary Fig. 2). To further analyze specific cell-types, clusters from the primary tSNE were subset. SubsetData was used to isolate nuclei from a specific cell-type, and ScaleData, RunPCA, RunTSNE, FindNeighbors, and FindClusters were performed on the subset data to produce a new Seurat object for each cell-type.

Cell-type-specific gene expression analysis

To determine the marker genes in any given cluster or subset cluster, either FindMarkers or FindAllMarkers was used. To determine the marker genes that produced transcriptionally distinct subset clusters, e.g., OL6, differential gene expression using MAST was performed (Finak et al. 2015).

Differential gene expression analysis

Differential gene expression analysis was performed using Seurat's implementation of MAST (Finak et al. 2015). For bulk analysis, all CTE clusters were analyzed against all control clusters. For cell-type-specific analysis, one cluster from CTE was analyzed against the corresponding cluster from control. *P*-values from differential expression were Bonferroni-corrected for multiple comparisons.

Gene ontology analysis

The set of all genes significantly differentially expressed between CTE and control nuclei (FDR < 0.05) within astrocyte cell-types were used as query inputs for gene ontology analyses by PANTHER Classification System v14.1 (www.pantherdb.org) to identify over-represented gene modules. Modules were assigned by PANTHER's statistical overrepresentation test in which a binomial test was applied to each query set relative to its corresponding reference gene set (all genes expressed in a certain cell-type) to determine if a known biological pathway had non-random linkage within the query set. All identified modules derived from PANTHER's "GO biological process complete" gene annotation and only those with a false-discovery-rate-corrected *P*-value < 0.05 were considered.

Cell-type representation analysis

To determine whether any cluster of nuclei was increased or decreased in CTE across all subjects, numbers of nuclei in each cluster were normalized to the sample with the largest number of nuclei (see methods in (Schirmer et al. 2019)). The following formulas for normalization were used:

$$\text{Sample normalization factor} = \frac{\text{Total nuclei in sample}}{\text{Total nuclei in sample with the largest number of nuclei}}$$

$$\text{Normalized nuclei count} = \frac{\text{Raw number of nuclei in a cluster}}{\text{Sample normalization factor}}$$

Normalized cell numbers for each cell-type and sample were then compared between conditions using a Mann-Whitney U test (FDR-corrected for multiple comparisons).

Iron staining

Fresh frozen tissue stored at -80° Celsius was adhered to cryostat compatible metal chucks using Optimal Cutting Temperature compound (Leica) and allowed to acclimate to a -17° Celsius cryostat (Leica CM3050 S) for 1 hour before cutting. Tissue was cut at 16µm thick sections and placed on Fisher Superfrost Plus (Fisher Scientific) slides. All slides were heated in a 60° Celsius oven for 15 minutes after cutting for tissue adherence and placed directly in room temperature 10% formalin for 1.5 hours for fixation. Slides were then dehydrated in 50%, 70%, and 100% ethanol baths for 2 minutes each before being heated in a 60° Celsius oven for 30 minutes to dry slides for room temperature storage. Prussian blue staining, which produces a dark blue pigment on all ferrous iron present in the tissue, was completed on all slides with hematoxylin and eosin counterstain. Prussian blue stained slides were placed in a solution of 0.06N Hydrochloric acid and Potassium Ferricyanide for 1 hour at room temperature before a wash in 1% Acetic Acid and hematoxylin and eosin counterstains.

Immunofluorescence

Fresh frozen tissue stored at -80° Celsius was adhered to cryostat compatible metal chucks using Optimal Cutting Temperature compound (Leica) and allowed to acclimate to a -17° Celsius cryostat (Leica CM3050 S) for 1 hour before cutting. Slides used for immunofluorescence staining were cut at 10µm using a CryoJane Tape Transfer System (Leica). Slides were placed in ice cold formalin for 15 minutes after cutting, rinsed in PBS, and allowed to dry fully under a ventilation hood. Slides were then stored at -80° Celsius and allowed to thaw at 4° Celsius before being used for manual immunofluorescent staining. Anti-mouse GFAP (1:1,000; Millipore) and anti-rabbit CD44 (1:2,000; Abcam) antibodies were used for double-labeled immunofluorescence staining. Slides were placed in 3 changes of 0.01% Triton for 5 minutes for tissue permeabilization, blocked in 3% normal donkey serum for 30 minutes, heated at 95° Celsius in AR6 solution (Perkin Elmer) for 20 minutes, and placed in a 4° Celsius refrigerator overnight with a primary antibody. A donkey anti-mouse or a donkey anti-rabbit secondary was used at a 1:500 concentration with 1% Normal Donkey Serum for one hour at room temperature. Fluorescent labeling was conducted using Opal

480 (GFAP) and Opal 570 (CD44) dyes (1:150; Perkin Elmer) for 10 minutes at room temperature, followed by 5 minutes of DAPI counterstaining.

Immunohistochemistry

Fresh frozen tissue stored at -80° Celsius was adhered to cryostat compatible metal chucks using Optimal Cutting Temperature compound (Leica) and allowed to acclimate to a -17° Celsius cryostat (Leica CM3050 S) for 1 hour before cutting. Tissue was cut at 16µm thick sections and placed on Fisher Superfrost Plus (Fisher Scientific) slides. All slides were heated in a 60° Celsius oven for 15 minutes after cutting for tissue adherence and placed directly in room temperature 10% formalin for 1.5 hours for fixation. Slides were then dehydrated in 50%, 70%, and 100% ethanol baths for 2 minutes each before being heated in a 60° Celsius oven for 30 minutes to dry slides for room temperature storage. All brightfield immunohistochemistry was completed using individually optimized protocols using Research Detection Kits on a BOND RX (Leica) system. Antibodies used on the BOND RX included: anti-rabbit PDGFRa (1:100; Abcam) and anti-rabbit OLIG2 (1:100; Millipore).

RNA in situ hybridization

Fresh frozen tissue stored at -80° Celsius was adhered to cryostat compatible metal chucks using Optimal Cutting Temperature compound (Leica) and allowed to acclimate to a -17° Celsius cryostat (Leica CM3050 S) for 1 hour before cutting. Tissue was cut at 16µm thick sections and placed on Fisher Superfrost Plus (Fisher Scientific) slides. All slides were heated in a 60° Celsius oven for 15 minutes after cutting for tissue adherence and placed directly in room temperature 10% formalin for 1.5 hours for fixation. Slides were then dehydrated in 50%, 70%, and 100% ethanol baths for 2 minutes each before being heated in a 60° Celsius oven for 30 minutes to dry slides for room temperature storage. RNA in situ hybridization was conducted using RNAscope (Advanced Cell Diagnostics) probes optimized for use on a BOND RX (Leica) system. All slides were treated with a 30 minute protease step, 1 minute of hybridization, and 10 minutes of epitope retrieval at the beginning and end of the protocol. Concentration of Opal dyes (480, 570, 690; Perkin Elmer) for fluorescent labeling were diluted at 1:1,500 in TSA Buffer (Advanced Cell Diagnostics) for every probe, all other steps were completed according to manufacturer's instructions.

Slide visualization and quantification

All slides used for iron staining, immunofluorescence, immunohistochemistry, and RNA in situ hybridization were scanned at 40X using custom protocols on a Vectra Polaris (Perkin Elmer) whole slide scanner and quantified using custom protocols on HALO (Indica Labs) software. All analyses were conducted in $1mm^2$ sections of the white matter tissue adjacent to the depth of a cortical sulcus unless otherwise specified.

Statistical analyses

Statistical analyses were performed in either R version 3.6.1 or Graphpad Prism 8. Gene expression statistical analyses were performed in R using MAST and Bonferroni correction for multiple

comparisons (Finak et al. 2015). To identify an increase or decrease in the number of normalized nuclei between conditions, a Mann-Whitney U test was performed, and *P*-values were FDR-corrected for multiple comparisons. Immunohistochemistry, immunofluorescence, and RNA in situ hybridization quantification was performed using a one-tailed Student's t-test or one-tailed Mann-Whitney U test. No statistical methods were used to predetermine sample size. Sample size was determined by tissue availability.

Data and code availability

Raw and processed data, as well as all code used for computational analyses will be made available upon publication of this manuscript.

Acknowledgments

We thank the VA-BU-CLF/UNITE Brain Bank and the National PTSD Brain Bank for providing human brain tissue; the Harvard Medical School Single Cell Core and the inDrops core facility for single nucleus RNA-seq sample preparation; and the Harvard Biopolymers Facility for sample quality control and RNA sequencing. This work was supported in part by the Harvard/MIT Basic Neuroscience Grants Program (K.B.C., J.E.D-C., A.C.M.) and the Concussion Legacy Foundation Young Investigator Fellowship (S.E.C.).

Author Contributions

K.B.C., S.E.C., and A.C.M. designed all experiments. B.R.H., T.D.S., V.E.A., and A.C.M. performed neuropathological evaluation of each subject. S.E.C. collected all tissue. K.B.C. performed snRNA-seq sample preparation. K.B.C., with assistance from J.E.D-C, performed computational analysis of the snRNA-seq data. S.E.C., with assistance from K.B.C., performed all in situ validation. K.B.C., S.E.C., and A.C.M. wrote the manuscript with input from the co-authors. K.B.C., S.E.C., and A.C.M. oversaw all aspects of the study.

References

Akila Parvathy Dharshini, S., Y-H Taguchi, and M. Michael Gromiha. 2019. "Exploring the Selective Vulnerability in Alzheimer Disease Using Tissue Specific Variant Analysis." *Genomics* 111 (4): 936–49.

Alosco, Michael L., Thor D. Stein, Yorghos Tripodis, Alicia S. Chua, Neil W. Kowall, Bertrand Russell Huber, Lee E. Goldstein, et al. 2019. "Association of White Matter Rarefaction, Arteriolosclerosis, and Tau With Dementia in Chronic Traumatic Encephalopathy." *JAMA Neurology*, August. https://doi.org/10.1001/jamaneurol.2019.2244.

Barbey, Aron K., Roberto Colom, and Jordan Grafman. 2013. "Dorsolateral Prefrontal Contributions to Human Intelligence." *Neuropsychologia* 51 (7): 1361–69.

Blondel, Vincent D., Jean-Loup Guillaume, Renaud Lambiotte, and Etienne Lefebvre. 2008. "Fast Unfolding of Communities in Large Networks." *Journal of Statistical Mechanics: Theory and Experiment*. https://doi.org/10.1088/1742-5468/2008/10/p10008.

Blumbergs, P. C., G. Scott, J. Manavis, H. Wainwright, D. A. Simpson, and A. J. McLean. 1994. "Staining of Amyloid Precursor Protein to Study Axonal Damage in Mild Head Injury." *The Lancet* 344 (8929): 1055–56.

Butler, Andrew, Paul Hoffman, Peter Smibert, Efthymia Papalexi, and Rahul Satija. 2018. "Integrating Single-Cell Transcriptomic Data across Different Conditions, Technologies, and Species." *Nature Biotechnology*, April. https://doi.org/10.1038/nbt.4096.

Chen, Tong, Wei-Ping Gai, and Catherine A. Abbott. 2014. "Dipeptidyl Peptidase 10 (DPP10789): A Voltage Gated Potassium Channel Associated Protein Is Abnormally Expressed in Alzheimer's and Other Neurodegenerative Diseases." *BioMed Research International* 2014.

Cherry, Jonathan D., Yorghos Tripodis, Victor E. Alvarez, Bertrand Huber, Patrick T. Kiernan, Daniel H. Daneshvar, Jesse Mez, et al. 2016. "Microglial Neuroinflammation Contributes to Tau Accumulation in Chronic Traumatic Encephalopathy." *Acta Neuropathologica Communications* 4 (1): 112.

Clarke, Laura E., Shane A. Liddelow, Chandrani Chakraborty, Alexandra E. Münch, Myriam Heiman, and Ben A. Barres. 2018. "Normal Aging Induces A1-like Astrocyte Reactivity." *Proceedings of the National Academy of Sciences of the United States of America* 115 (8): E1896–1905.

Critchley, M. 1949. *Punch-Drunk Syndromes: The Chronic Traumatic Encephalopathy of Boxers*. Maloine. Paris: Hommage a Clovis Vincent.

Doherty, Colin P., Eoin O'Keefe, Eugene Wallace, Teresa Loftus, James Keaney, John Kealy, Marian M. Humphries, et al. 2016. "Blood-Brain Barrier Dysfunction as a Hallmark Pathology in Chronic Traumatic Encephalopathy." *Journal of Neuropathology and Experimental Neurology* 75 (7): 656–62.

Falcão, Ana Mendanha, David van Bruggen, Sueli Marques, Mandy Meijer, Sarah Jäkel, Eneritz Agirre, Samudyata, et al. 2018. "Disease-Specific Oligodendrocyte Lineage Cells Arise in Multiple Sclerosis." *Nature Medicine*, November, 1.

Finak, Greg, Andrew McDavid, Masanao Yajima, Jingyuan Deng, Vivian Gersuk, Alex K. Shalek, Chloe K. Slichter, et al. 2015. "MAST: A Flexible Statistical Framework for Assessing Transcriptional Changes and Characterizing Heterogeneity in Single-Cell RNA Sequencing Data." *Genome Biology* 16 (December): 278.

Foster, Evangeline M., Adrià Dangla-Valls, Simon Lovestone, Elena M. Ribe, and Noel J. Buckley. 2019. "Clusterin in Alzheimer's Disease: Mechanisms, Genetics, and Lessons From Other Pathologies." *Frontiers in Neuroscience*. https://doi.org/10.3389/fnins.2019.00164.

Funahashi, Shintaro, and Jorge Mario Andreau. 2013. "Prefrontal Cortex and Neural Mechanisms of Executive Function." *Journal of Physiology, Paris* 107 (6): 471–82.

Grubman, Alexandra, Gabriel Chew, John F. Ouyang, Guizhi Sun, Xin Yi Choo, Catriona McLean, Rebecca K. Simmons, et al. 2019. "A Single-Cell Atlas of Entorhinal Cortex from Individuals with Alzheimer's Disease Reveals Cell-Type-Specific Gene Expression Regulation." *Nature Neuroscience* 22 (12): 2087–97.

Habib, Naomi, Inbal Avraham-Davidi, Anindita Basu, Tyler Burks, Karthik Shekhar, Matan Hofree, Sourav R. Choudhury, et al. 2017. "Massively Parallel Single-Nucleus RNA-Seq with DroNc-Seq." *Nature Methods* 14 (10): 955–58.

Hafemeister, Christoph, and Rahul Satija. 2019. "Normalization and Variance Stabilization of Single-Cell RNA-Seq Data Using Regularized Negative Binomial Regression." *Genome Biology* 20 (1): 296.

Holleran, Laurena, Joong Hee Kim, Mihika Gangolli, Thor Stein, Victor Alvarez, Ann McKee, and David L. Brody. 2017. "Axonal Disruption in White Matter Underlying Cortical Sulcus Tau Pathology in Chronic Traumatic Encephalopathy." *Acta Neuropathologica* 133 (3): 367–80.

Hrvatin, Sinisa, Daniel R. Hochbaum, M. Aurel Nagy, Marcelo Cicconet, Keiramarie Robertson, Lucas Cheadle, Rapolas Zilionis, et al. 2018. "Single-Cell Analysis of Experience-Dependent Transcriptomic States in the Mouse Visual Cortex." *Nature Neuroscience* 21 (1): 120–29.

Hsu, Eric T., Mihika Gangolli, Shiran Su, Laurena Holleran, Thor D. Stein, Victor E. Alvarez, Ann C. McKee, Robert E. Schmidt, and David L. Brody. 2018. "Astrocytic Degeneration in Chronic Traumatic Encephalopathy." *Acta Neuropathologica*, September. https://doi.org/10.1007/s00401-018-1902-3.

Iancu, T. C. 1992. "Ferritin and Hemosiderin in Pathological Tissues." *Electron Microscopy Reviews* 5 (2): 209–29.

Jäkel, Sarah, Eneritz Agirre, Ana Mendanha Falcão, David van Bruggen, Ka Wai Lee, Irene Knuesel, Dheeraj Malhotra, Charles ffrench-Constant, Anna Williams, and Gonçalo Castelo-Branco. 2019. "Altered Human Oligodendrocyte Heterogeneity in Multiple Sclerosis." *Nature*, January. https://doi.org/10.1038/s41586-019-0903-2.

Jha, Mithilesh Kumar, Sangmin Jeon, and Kyoungho Suk. 2012. "Pyruvate Dehydrogenase Kinases in the Nervous System: Their Principal Functions in Neuronal-Glial Metabolic Interaction and Neuro-Metabolic Disorders." *Current Neuropharmacology* 10 (4): 393–403.

Klein, Allon M., Linas Mazutis, Ilke Akartuna, Naren Tallapragada, Adrian Veres, Victor Li, Leonid Peshkin, David A. Weitz, and Marc W. Kirschner. 2015. "Droplet Barcoding for Single-Cell Transcriptomics Applied to Embryonic Stem Cells." *Cell* 161 (5): 1187–1201.

Kobak, Dmitry, and Philipp Berens. 2019. “The Art of Using T-SNE for Single-Cell Transcriptomics.” *Nature Communications* 10 (1): 5416.

Koenigs, Michael, and Jordan Grafman. 2009. “The Functional Neuroanatomy of Depression: Distinct Roles for Ventromedial and Dorsolateral Prefrontal Cortex.” *Behavioural Brain Research* 201 (2): 239–43.

Kruer, Michael C., Coro Paisán-Ruiz, Nathalie Boddaert, Moon Y. Yoon, Hiroko Hama, Allison Gregory, Alessandro Malandrini, et al. 2010. “Defective FA2H Leads to a Novel Form of Neurodegeneration with Brain Iron Accumulation (NBIA).” *Annals of Neurology* 68 (5): 611–18.

Liddelow, Shane A., and Ben A. Barres. 2017. “Reactive Astrocytes: Production, Function, and Therapeutic Potential.” *Immunity* 46 (6): 957–67.

Liddelow, Shane A., Kevin A. Guttenplan, Laura E. Clarke, Frederick C. Bennett, Christopher J. Bohlen, Lucas Schirmer, Mariko L. Bennett, et al. 2017. “Neurotoxic Reactive Astrocytes Are Induced by Activated Microglia.” *Nature* 541 (7638): 481–87.

Lu, Liyan, Heli Cao, Xiaoer Wei, Yuehua Li, and Wenbin Li. 2015. “Iron Deposition Is Positively Related to Cognitive Impairment in Patients with Chronic Mild Traumatic Brain Injury: Assessment with Susceptibility Weighted Imaging.” *BioMed Research International* 2015 (December): 470676.

Maaten, Laurens van der, and Geoffrey Hinton. 2008. “Visualizing Data Using T-SNE.” *Journal of Machine Learning Research: JMLR* 9 (Nov): 2579–2605.

Mahar, Ian, Michael L. Alosco, and Ann C. McKee. 2017. “Psychiatric Phenotypes in Chronic Traumatic Encephalopathy.” *Neuroscience and Biobehavioral Reviews* 83 (December): 622–30.

Mariani, S., M. Ventriglia, I. Simonelli, G. Spalletta, S. Bucossi, M. Siotto, F. Assogna, J. M. Melgari, F. Vernieri, and R. Squitti. 2013. “Effects of Hemochromatosis and Transferrin Gene Mutations on Peripheral Iron Dyshomeostasis in Mild Cognitive Impairment and Alzheimer’s and Parkinson's Diseases.” *Frontiers in Aging Neuroscience*. https://doi.org/10.3389/fnagi.2013.00037.

Martland, Harrison S. 1928. “PUNCH DRUNK.” *JAMA: The Journal of the American Medical Association* 91 (15): 1103–7.

Mathys, Hansruedi, Jose Davila-Velderrain, Zhuyu Peng, Fan Gao, Shahin Mohammadi, Jennie Z. Young, Madhvi Menon, et al. 2019. “Single-Cell Transcriptomic Analysis of Alzheimer’s Disease.” *Nature* 570 (7761): 332–37.

McCarthy, Davis J., Kieran R. Campbell, Aaron T. L. Lun, and Quin F. Wills. 2017. “Scater: Pre-Processing, Quality Control, Normalization and Visualization of Single-Cell RNA-Seq Data in R.” *Bioinformatics* 33 (8): 1179–86.

McKee, Ann C., Nigel J. Cairns, Dennis W. Dickson, Rebecca D. Folkerth, C. Dirk Keene, Irene Litvan, Daniel P. Perl, et al. 2016. "The First NINDS/NIBIB Consensus Meeting to Define Neuropathological Criteria for the Diagnosis of Chronic Traumatic Encephalopathy." *Acta Neuropathologica* 131 (1): 75–86.

McKee, Ann C., Robert C. Cantu, Christopher J. Nowinski, E. Tessa Hedley-Whyte, Brandon E. Gavett, Andrew E. Budson, Veronica E. Santini, Hyo-Soon Lee, Caroline A. Kubilus, and Robert A. Stern. 2009. "Chronic Traumatic Encephalopathy in Athletes: Progressive Tauopathy After Repetitive Head Injury." *Journal of Neuropathology and Experimental Neurology* 68 (7): 709–35.

McKee, Ann C., Daniel H. Daneshvar, Victor E. Alvarez, and Thor D. Stein. 2014. "The Neuropathology of Sport." *Acta Neuropathologica*. https://doi.org/10.1007/s00401-013-1230-6.
McKee, Ann C., Thor D. Stein, Patrick T. Kiernan, and Victor E. Alvarez. 2015. "The Neuropathology of Chronic Traumatic Encephalopathy." *Brain Pathology* 25 (3): 350–64.

McKee, Ann C., Thor D. Stein, Christopher J. Nowinski, Robert A. Stern, Daniel H. Daneshvar, Victor E. Alvarez, Hyo-Soon Lee, et al. 2013. "The Spectrum of Disease in Chronic Traumatic Encephalopathy." *Brain: A Journal of Neurology* 136 (1): 43–64.

Mez, Jesse, Daniel H. Daneshvar, Patrick T. Kiernan, Bobak Abdolmohammadi, Victor E. Alvarez, Bertrand R. Huber, Michael L. Alosco, et al. 2017. "Clinicopathological Evaluation of Chronic Traumatic Encephalopathy in Players of American Football." *JAMA - Journal of the American Medical Association* 318 (4): 360–70.

Montenigro, Philip H., Christine M. Baugh, Daniel H. Daneshvar, Jesse Mez, Andrew E. Budson, Rhoda Au, Douglas I. Katz, Robert C. Cantu, and Robert A. Stern. 2014. "Clinical Subtypes of Chronic Traumatic Encephalopathy: Literature Review and Proposed Research Diagnostic Criteria for Traumatic Encephalopathy Syndrome." *Alzheimer's Research and Therapy*. BioMed Central Ltd. https://doi.org/10.1186/s13195-014-0068-z.

Munro, H. N. 1990. "Iron Regulation of Ferritin Gene Expression." *Journal of Cellular Biochemistry* 44 (2): 107–15.

Nagy, Corina, Malosree Maitra, Arnaud Tanti, Matthew Suderman, Jean-Francois Théroux, Maria Antonietta Davoli, Kelly Perlman, et al. 2020. "Single-Nucleus Transcriptomics of the Prefrontal Cortex in Major Depressive Disorder Implicates Oligodendrocyte Precursor Cells and Excitatory Neurons." *Nature Neuroscience*, April. https://doi.org/10.1038/s41593-020-0621-y.

Nisenbaum, Eric J., Dmitry S. Novikov, and Yvonne W. Lui. 2014. "The Presence and Role of Iron in Mild Traumatic Brain Injury: An Imaging Perspective." *Journal of Neurotrauma* 31 (4): 301–7.

Omalu, Bennet I., Steven T. DeKosky, Ronald L. Hamilton, Ryan L. Minster, M. Ilyas Kamboh, Abdulrezak M. Shakir, and Cyril H. Wecht. 2006. "Chronic Traumatic Encephalopathy in a National Football League Player: Part II." *Neurosurgery* 59 (5): 1086–92; discussion 1092–93.

Omalu, Bennet I., Steven T. DeKosky, Ryan L. Minster, M. Ilyas Kamboh, Ronald L. Hamilton, and Cyril H. Wecht. 2005. "Chronic Traumatic Encephalopathy in a National Football League Player." *Neurosurgery* 57 (1): 128–34; discussion 128–34.

Oppenheimer, D. R. 1968. "Microscopic Lesions in the Brain Following Head Injury." *Journal of Neurology, Neurosurgery, and Psychiatry* 31 (4): 299–306.

Ousman, Shalina S., Beren H. Tomooka, Johannes M. van Noort, Eric F. Wawrousek, Kevin C. O'Connor, David A. Hafler, Raymond A. Sobel, William H. Robinson, and Lawrence Steinman. 2007. "Protective and Therapeutic Role for alphaB-Crystallin in Autoimmune Demyelination." *Nature* 448 (7152): 474–79.

Raz, E., J. H. Jensen, Y. Ge, J. S. Babb, L. Miles, J. Reaume, R. I. Grossman, and M. Inglese. 2011. "Brain Iron Quantification in Mild Traumatic Brain Injury: A Magnetic Field Correlation Study." *AJNR. American Journal of Neuroradiology* 32 (10): 1851–56.

Rowatt, Katelyn, Rachel E. Burns, Salvatore Frasca, and Denise M. Long. 2018. "A Combination Prussian Blue – Hematoxylin and Eosin Staining Technique for Identification of Iron and Other Histological Features." *Journal of Histotechnology*. https://doi.org/10.1080/01478885.2017.1417696.

Sala, M., E. Caverzasi, M. Lazzaretti, N. Morandotti, G. De Vidovich, E. Marraffini, F. Gambini, et al. 2011. "Dorsolateral Prefrontal Cortex and Hippocampus Sustain Impulsivity and Aggressiveness in Borderline Personality Disorder." *Journal of Affective Disorders* 131 (1-3): 417–21.

Schirmer, Lucas, Dmitry Velmeshev, Staffan Holmqvist, Max Kaufmann, Sebastian Werneburg, Diane Jung, Stephanie Vistnes, et al. 2019. "Neuronal Vulnerability and Multilineage Diversity in Multiple Sclerosis." *Nature*. https://doi.org/10.1038/s41586-019-1404-z.

Seo, Jeong-Sun, Seungbok Lee, Jong-Yeon Shin, Yu Jin Hwang, Hyesun Cho, Seong-Keun Yoo, Yunha Kim, et al. 2017. "Transcriptome Analyses of Chronic Traumatic Encephalopathy Show Alterations in Protein Phosphatase Expression Associated with Tauopathy." *Experimental & Molecular Medicine* 49 (5): e333.

Simon, Matthew J., Marie X. Wang, Charles F. Murchison, Natalie E. Roese, Erin L. Boespflug, Randall L. Woltjer, and Jeffrey J. Iliff. 2018. "Transcriptional Network Analysis of Human Astrocytic Endfoot Genes Reveals Region-Specific Associations with Dementia Status and Tau Pathology." *Scientific Reports* 8 (1): 12389.

Stern, Robert A., Daniel H. Daneshvar, Christine M. Baugh, Daniel R. Seichepine, Philip H. Montenigro, David O. Riley, Nathan G. Fritts, et al. 2013. "Clinical Presentation of Chronic Traumatic Encephalopathy." *Neurology* 81 (13): 1122–29.

Stockwell, Brent R., José Pedro Friedmann Angeli, Hülya Bayir, Ashley I. Bush, Marcus Conrad, Scott J. Dixon, Simone Fulda, et al. 2017. "Ferroptosis: A Regulated Cell Death Nexus Linking Metabolism, Redox Biology, and Disease." *Cell* 171 (2): 273–85.

Tagge, Chad A., Andrew M. Fisher, Olga V. Minaeva, Amanda Gaudreau-Balderrama, Juliet A. Moncaster, Xiao-Lei Zhang, Mark W. Wojnarowicz, et al. 2018. "Concussion, Microvascular Injury, and Early Tauopathy in Young Athletes after Impact Head Injury and an Impact Concussion Mouse Model." *Brain: A Journal of Neurology* 141 (2): 422–58.

Velmeshev, Dmitry, Lucas Schirmer, Diane Jung, Maximilian Haeussler, Yonatan Perez, Simone Mayer, Aparna Bhaduri, Nitasha Goyal, David H. Rowitch, and Arnold R. Kriegstein. 2019. "Single-Cell Genomics Identifies Cell Type–specific Molecular Changes in Autism." *Science*. https://doi.org/10.1126/science.aav8130.

Vidal, R., B. Ghetti, M. Takao, C. Brefel-Courbon, E. Uro-Coste, B. S. Glazier, V. Siani, et al. 2004. "Intracellular Ferritin Accumulation in Neural and Extraneural Tissue Characterizes a Neurodegenerative Disease Associated with a Mutation in theFerritin Light PolypeptideGene." *Journal of Neuropathology & Experimental Neurology*. https://doi.org/10.1093/jnen/63.4.363.

Zhang, Junfei, Jia Liu, Jiali Wu, Wenfeng Li, Zhongwei Chen, and Lishan Yang. 2019. "Progression of the Role of CRYAB in Signaling Pathways and Cancers." *OncoTargets and Therapy* 12 (May): 4129–39.

Zilionis, Rapolas, Juozas Nainys, Adrian Veres, Virginia Savova, David Zemmour, Allon M. Klein, and Linas Mazutis. 2017. "Single-Cell Barcoding and Sequencing Using Droplet Microfluidics." *Nature Protocols* 12 (1): 44–73.

Figure Legends

Supplementary Table 1: Demographic and clinical profiles of subjects

Figure 1. Overview of snRNA-seq and experimental approach. a. Cartoon of dorsolateral frontal white matter and white matter at the depth of a cortical sulcus taken for snRNA-seq analysis and in situ validation analyses. Dounce homogenizer used to dissociate tissue. Inverted microscope used by the inDrops core facility for single nucleus hydrogel encapsulation. Sequencer and example data produced by the snRNA-seq workflow. **b. (left)** Unbiased tSNE projection showing all major cell-types expected in human brain tissue. **(middle)** tSNE colored by condition, red: Control, teal: CTE. **(right)** tSNE colored by subject. Each subject is a different color, as shown by the figure key below. **c.** tSNE projection of each major cell type colored by expression of canonical marker genes: *PLP1* for oligodendrocytes, *GFAP* for astrocytes, *VCAN* for OPCs, *CD74* for microglia, *NRGN* for excitatory neurons, and *GAD1* for interneurons. Nuclei clusters positive for each marker gene are circled by a dashed line. **d.** Bubble plot of normalized number of nuclei with each subject in the data set on the y-axis and each cell-type and subpopulation on the x-axis. Size of the bubble indicates the number of normalized nuclei in each cell-type for each subject. Statistical analysis for significantly increased or decreased nuclei subpopulations listed at top (FDR-corrected Mann-Whitney U test). **e.** Violin plots of log-normalized counts for top expressed

genes identified by bulk (all control nuclei vs. all CTE nuclei) differential gene expression between conditions.

Supplementary Figure 1 (related to Figure 1). Tissue collection and quality control. a. Image of dorsolateral frontal white matter and depth of a cortical sulcus representing the region of tissue used for this project. Dashed rectangle represents a region taken for snRNA-seq analysis (only white matter at the depth of a cortical sulcus), solid rectangle represents a region taken for all in situ validation (gray and white matter adjacent to the region taken for snRNA-seq). GM: gray matter, WM: white matter, CS: cortical sulcus. **b.** Scatter plot with bar for each subject by age (P = 0.90, Mann-Whitney U test). **c.** Scatter plot with bar for each subject by post-mortem interval (PMI) (P = 0.25, Mann-Whitney U test). **d.** Scatter plot with bar for each subject by RNA integrity number (RIN) value (P = 0.72, Mann-Whitney U test). **e.** tSNE projection colored by number of genes present in each nucleus. **f.** tSNE projection colored by number of unique molecular identifiers (UMIs) present in each nucleus. **g. (left)** Violin plots for the number of genes expressed in each nucleus for control and CTE subjects. **(right)** Violin plots for the number of UMIs present in each nucleus for control and CTE subjects. **h.** Elbow plot for the amount of variance produced by each principal component. Principal components (PCs) from 1 to 30 on the x-axis and standard deviation on the y-axis.

Figure 2. Global loss of oligodendrocytes in CTE white matter.
a. tSNE projection of mature oligodendrocyte lineage nuclei subset from primary tSNE projection from Fig. 1b. **b.** Scatter plot with bar for normalized nuclei counts for all oligodendrocyte lineage nuclei, each dot represents the total normalized number of oligodendrocyte nuclei in one subject (P = 0.01, FDR-corrected Mann-Whitney U test). **c.** Representative immunohistochemistry images of control and CTE tissue stained with anti-OLIG2 for oligodendrocyte lineage cells. Scale bar **(top, white)**: 100µm. Quantification **(bottom)** for number of OLIG2-positive nuclei per mm^2 over the entire white matter sample for each subject (P = 0.04, one-tailed Student's t-test). **d.** Representative RNA in situ hybridization images for *OLIG2* (green) and DAPI (blue). Scale bar **(top, white)**: 50µm. Quantification **(bottom)** for number of *OLIG2*-positive nuclei for each subject (P = 0.02, one-tailed Student's t-test). **e.** Scatter plot for average gene expression in oligodendrocyte lineage nuclei. Control gene expression across the x-axis, CTE gene expression across the y-axis. *FTH1* and *CRYAB* are labeled as top differentially expressed genes between conditions.

Supplementary Figure 2 (related to Figure 1). Cell-type-specific marker gene expression. Dotplot with cell types on the x-axis and marker genes on the y-axis. Size of dot relates to the percent of nuclei in a given cluster that express the corresponding marker gene. Color of dot relates to the average marker gene expression for the nuclei expressing the marker gene in a given cluster.

Supplementary Figure 3 (related to Figure 2). Validation of global loss of oligodendrocytes in CTE white matter. a. Representative immunohistochemistry images for control and CTE stained with anti-OLIG2 for oligodendrocyte lineage cells. Scale bar **(top-left, white)**: 100µm. **b.** Immunohistochemistry images from main text **(top)** and the same images with masks **(bottom)** to demonstrate how positive cells are identified. Scale bar **(top-left, white)**: 100µm. **c.** Representative RNA in situ hybridization images for *OLIG2* (green) and DAPI (blue). Scale bar **(top-left, white)**: 50µm. **d.** RNA in situ hybridization images from main text **(top)** and the same

images with masks **(bottom)** to demonstrate how nuclei and positivity are identified. Scale bar **(top-left, white)**: 50µm.

Supplementary Figure 4 (related to Figure 2). OPC cell numbers do not change between conditions. a. tSNE projection of oligodendrocyte precursor cell nuclei subset from primary tSNE from Fig. 1b. **b.** Scatter plot with bar for normalized nuclei counts for all oligodendrocyte precursor cell nuclei, each dot represents the total normalized number of oligodendrocyte precursor cell nuclei in one subject (P = 0.13, FDR-corrected Mann-Whitney U test). **c.** Representative immunohistochemistry images for control and CTE stained with anti-PDGFRa for oligodendrocyte precursor cells. Scale bar (**top, black**): 100µm. Quantification **(right)** for number of PDGFRa-positive cells per mm^2 over the entire white matter sample for each subject (P = 0.23, one-tailed Student's t-test).

Figure 3. Iron accumulation in CTE-specific oligodendrocytes. a. tSNE projection of mature oligodendrocyte lineage nuclei subset from primary tSNE from Fig. 1b with CTE-specific subpopulations circled. **b.** Scatter plot with bar for normalized nuclei counts for CTE-specific oligodendrocyte subpopulations, each dot represents one subject (OL6: P = 0.001, OL7: P = 0.01, OL8: P = 0.05; FDR-corrected Mann-Whitney U test). **c.** Violin plots of log-normalized counts for top expressed genes in CTE-specific oligodendrocytes. **d.** Scatter plot for average gene expression in OL6. Control gene expression across the x-axis, CTE gene expression across the y-axis. *FTH1* and *CRYAB* are labeled as top differentially expressed genes between conditions. **e.** Representative images of Prussian blue staining for control and CTE tissue. Black arrows label iron inclusions. Scale bar **(left, white)**: 100µm. Quantification **(right)** for total iron inclusion count, each dot represents a subject (P = 0.04, one-tailed Student's t-test). **f.** Representative RNA in situ hybridization images for *OLIG2* (green), *FTH1* (yellow), *CRYAB* (red), and DAPI (blue). *OLIG2* and DAPI **(left)**, *FTH1* and DAPI **(middle-left)**, *CRYAB* and DAPI **(middle-right)**, and merge of all probes **(right)**. White arrows label nuclei positive for *OLIG2*, *FTH1*, *CRYAB*, and DAPI. Scale bar **(top-left, white)**: 50µm.

Supplementary Figure 5 (related to Figure 3). Validation of iron accumulation in CTE-specific oligodendrocytes. a. Representative images of Prussian blue staining for control and CTE. Black arrows label iron inclusions. Scale bar **(top-left, white)**: 100µm. **b.** Prussian blue images from main text **(top)** and the same images with masks to demonstrate how iron inclusions are identified **(bottom)**. Scale bar **(top-left, white)**: 100µm. **c.** Representative RNA in situ hybridization images for *OLIG2* (green), *FTH1* (yellow), *CRYAB* (red), and DAPI (blue). White arrows label nuclei positive for *OLIG2*, *FTH1*, *CRYAB*, and DAPI. Scale bar **(top-left, white)**: 50µm.

Figure 4. Neuroinflammatory astrocytes in CTE white matter. a. tSNE projection of astrocyte nuclei subset from primary tSNE from Fig. 1b. **b.** Scatter plot with bar for normalized nuclei counts for astrocyte subpopulations, each dot represents one subject (Astrocyte1: P = 0.02, Astrocyte2: P = 0.01, Astrocyte3: P = 0.03; FDR-corrected Mann-Whitney U test). **c.** Violin plots of log-normalized counts for top expressed genes in CTE-specific astrocytes. **d.** tSNE projection of subset astrocytes colored by expression of either *CD44*, *BCL6*, or *GFAP*. Astrocyte 3 circled. **e.** Representative immunofluorescence images for GFAP (teal), CD44 (yellow), and DAPI (blue) in control and CTE. Scale bar **(left, white)**: 100µm. Quantification **(right)** for percent of total area

positive for CD44 immunofluorescence for each subject (P = 0.02, one-tailed Student's t-test). **f.** Representative RNA in situ hybridization images for *GFAP* (teal), *CD44* (yellow), *BCL6* (red), and DAPI (blue). *GFAP* and DAPI **(left)**, *CD44* and DAPI **(middle-left)**, *BCL6* and DAPI **(middle-right)**, and merge of all probes **(right)**. White arrows label nuclei positive for *GFAP*, *CD44*, *BCL6*, and DAPI. Scale bar **(top-left, white)**: 50µm. Quantification **(right)** for the average intensity of *BCL6* positivity per *BCL6*-positive nuclei (P = 0.06, one-tailed Student's t-test). **g.** Top 10 enriched gene ontology terms ranked by FDR.

Supplementary Figure 6 (related to Figure 4). Astrocyte cell numbers do not change between conditions. a. tSNE projection of astrocyte nuclei subset from primary tSNE from Fig. 1b. **b.** Scatter plot with a bar for normalized nuclei counts for all astrocytes, each dot represents the total normalized number of astrocyte nuclei in one subject (P = 0.29, FDR-corrected Mann-Whitney U test). **c.** Representative immunofluorescence images for GFAP (teal) and DAPI (blue) in control and CTE. Scale bar **(left)**: 100µm. Quantification **(right)** for percent of total area positive for GFAP immunofluorescence for each subject (P = 0.44, one-tailed Student's t-test). **d. (top)** Representative RNA in situ hybridization images for *GFAP* (teal) and DAPI (blue). **(bottom)** Same images as top but with masks to demonstrate how nuclei and positivity are identified. Scale bar **(top-left, white)**: 50µm. Quantification **(right)** for number of *GFAP*-positive nuclei for each subject (P = 0.50, one-tailed Mann Whitney U-test).

Supplementary Figure 7 (related to Figure 4). Validation of neuroinflammatory astrocytes in CTE white matter. a. Representative immunofluorescence images for GFAP (teal), CD44 (yellow), and DAPI (blue) in control and CTE. Scale bar **(top-left, white)**: 100µm. **b.** Immunofluorescence images from main text **(top)** and the same images with masks **(bottom)** to demonstrate how GFAP and CD44 positivity are identified. Scale bar **(top-left, white)**: 100µm. **c.** Representative RNA in situ hybridization images for *GFAP* (teal), *CD44* (yellow), *BCL6* (red), and DAPI (blue) in control and CTE. White arrows label nuclei positive for *GFAP*, *CD44*, *BCL6*, and DAPI. Scale bar **(top-left, white)**: 50µm. **d.** RNA in situ hybridization images for *GFAP* (teal), *CD44* (yellow), *BCL6* (red), and DAPI (blue) in control and CTE **(top)** and the same images with masks **(bottom)** to demonstrate how nuclei and *BCL6* positivity are identified. Scale bar **(top-left, white)**: 50µm.

Figure 1. Overview of snRNA-seq and experimental approach

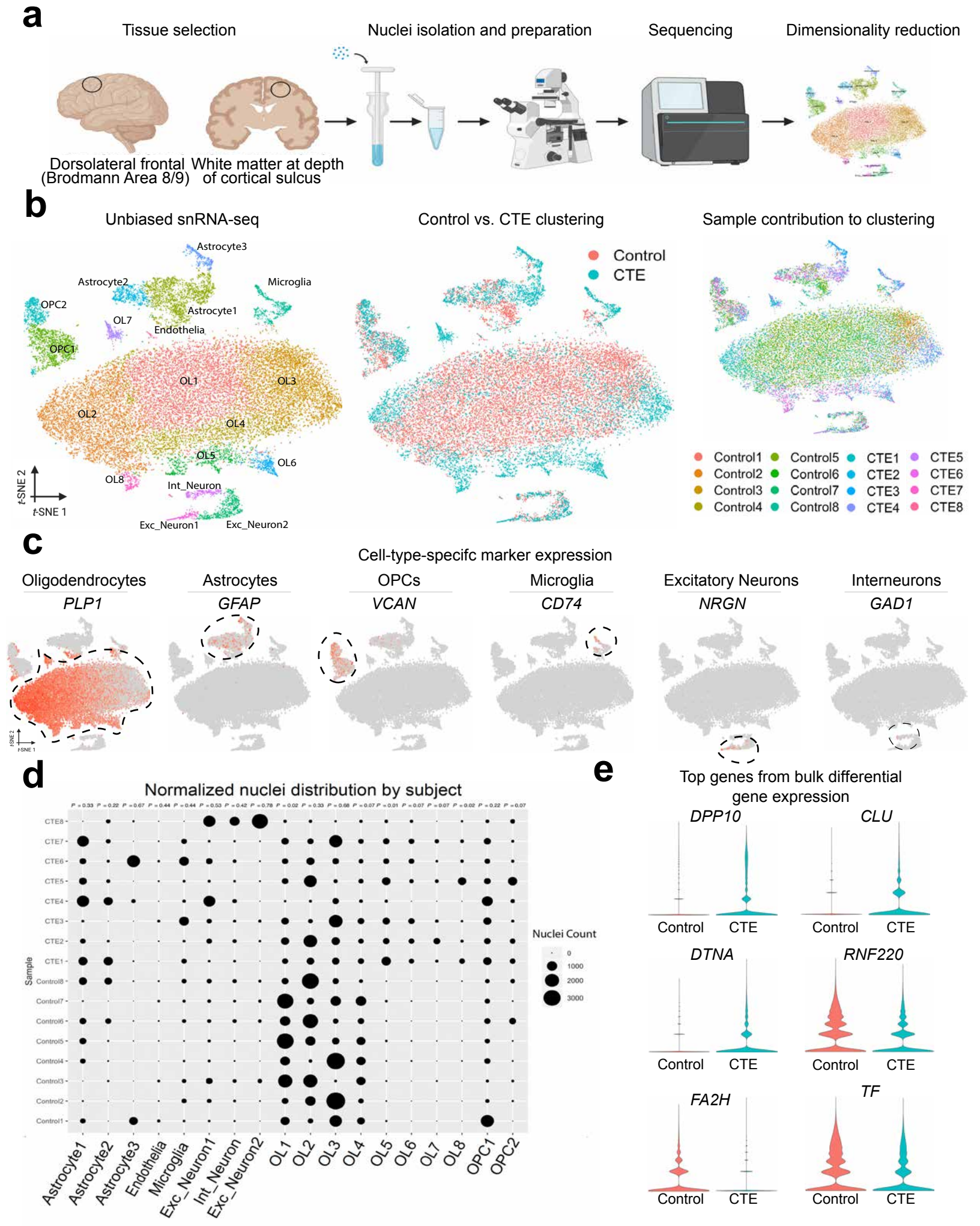

Supplementary Figure 1 (related to Figure 1): Tissue collection and quality control

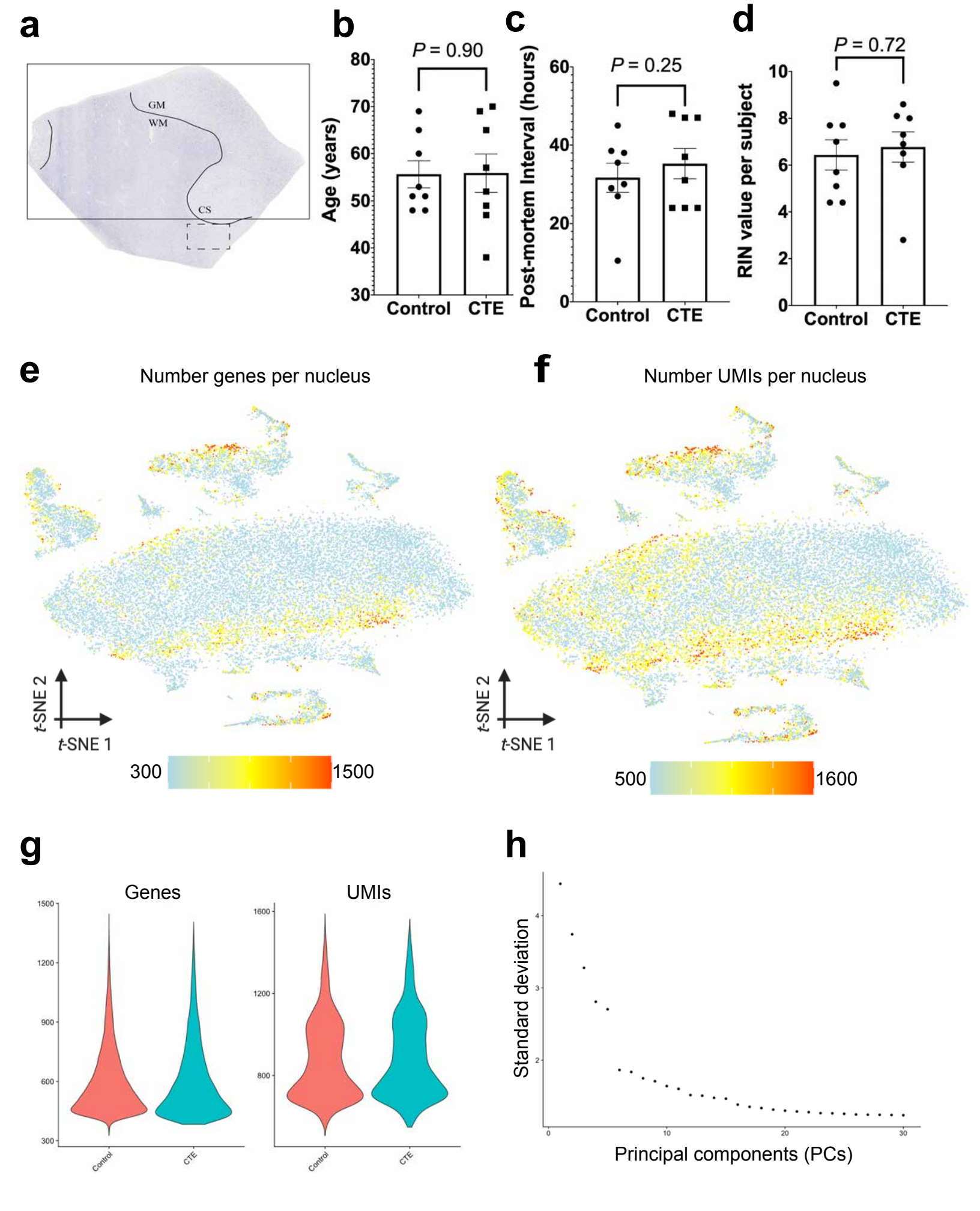

Supplementary Figure 2 (related to Figure 1): Cell-type-specific marker gene expression

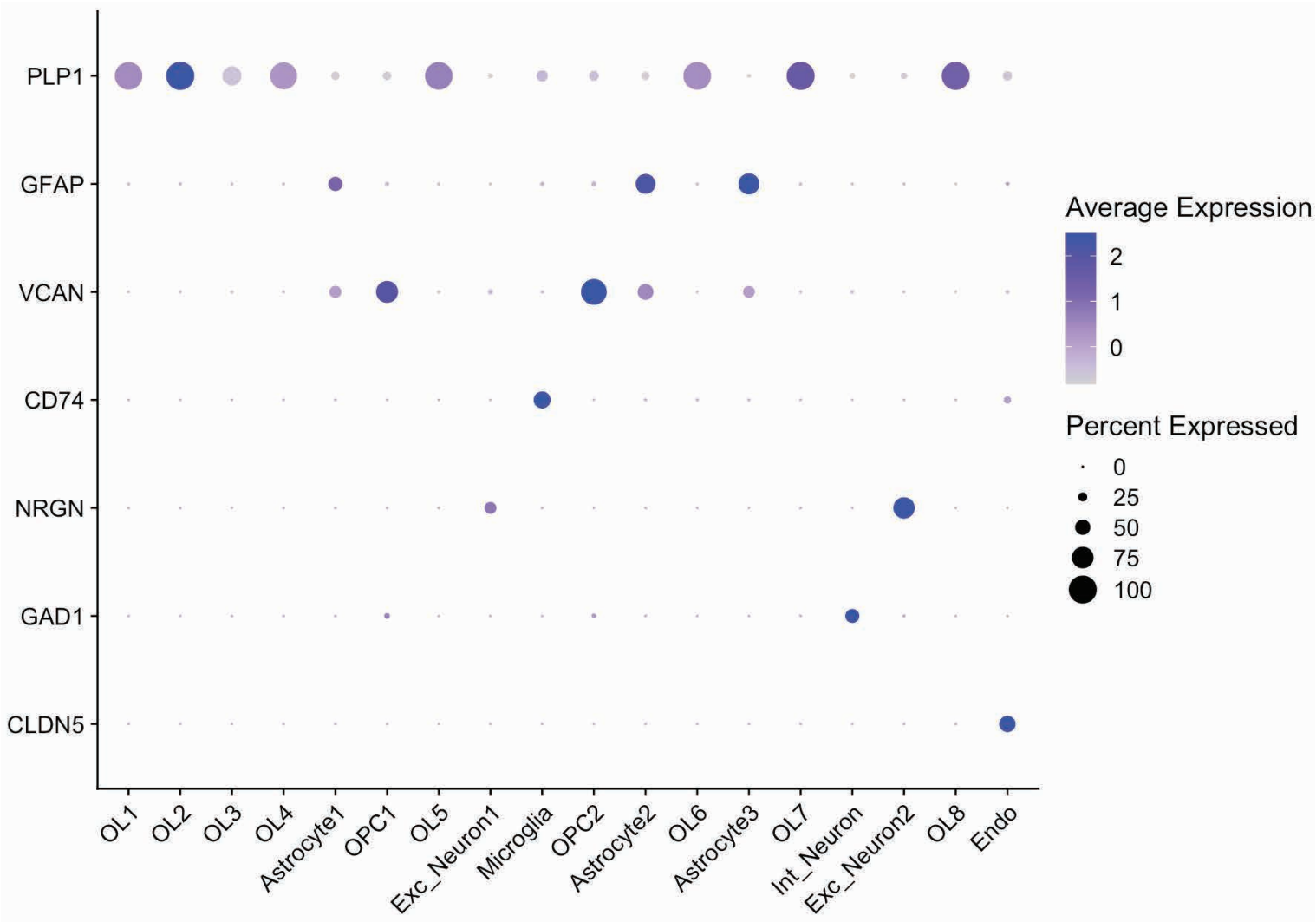

Figure 2. Global loss of oligodendrocytes in CTE white matter.

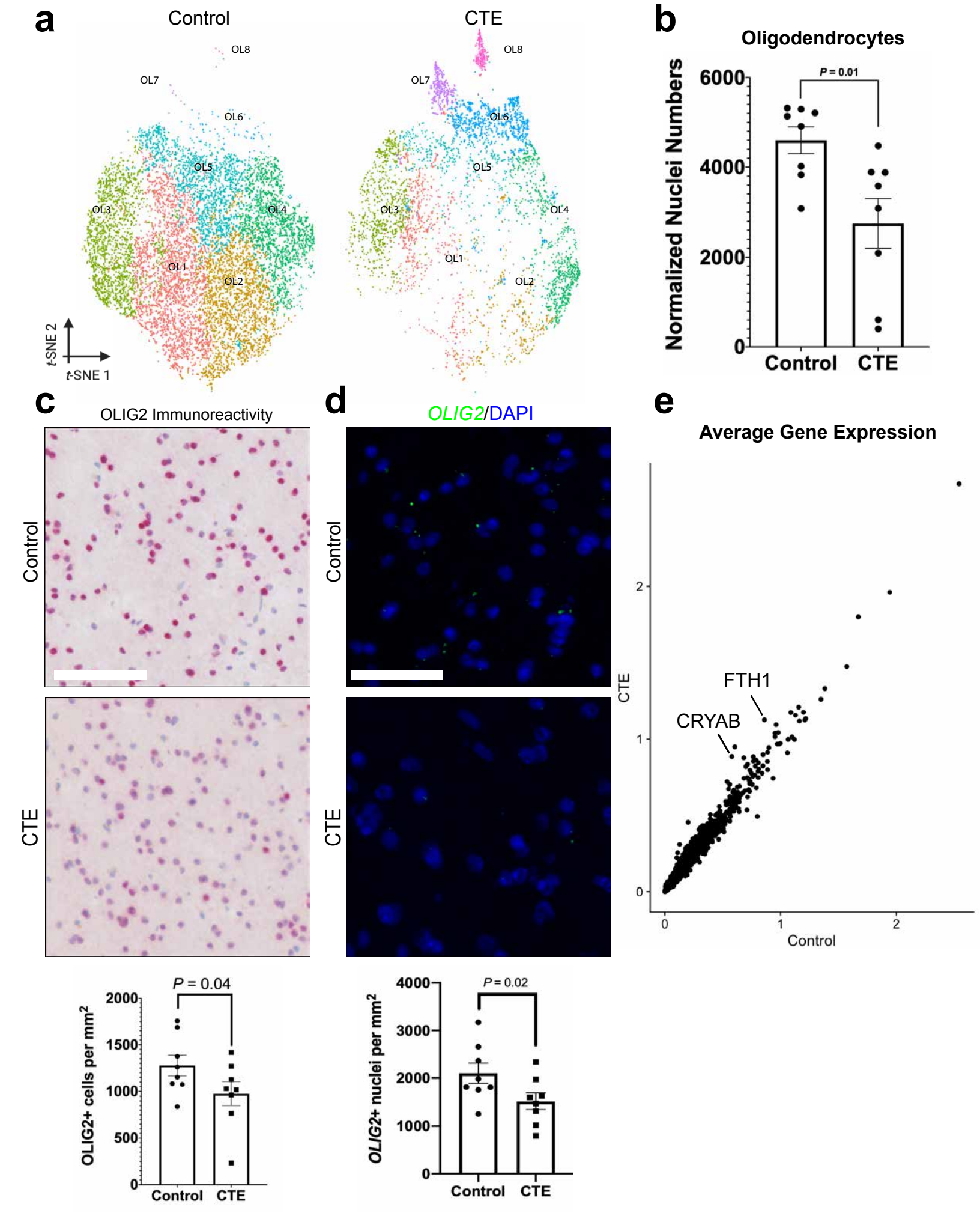

Supplementary Figure 3 (related to Figure 2): Validation of global loss of oligodendrocytes in CTE white matter

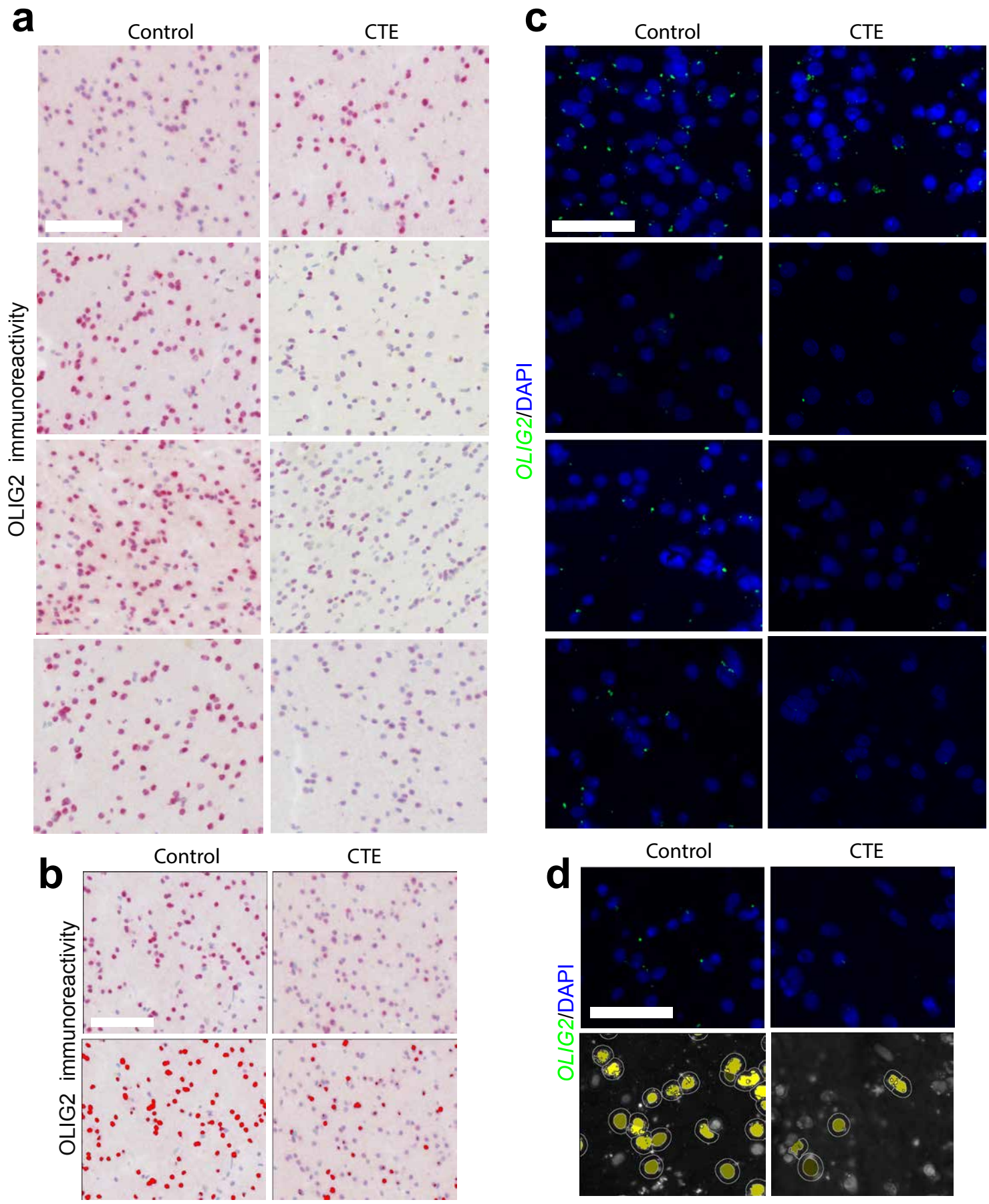

Supplementary Figure 4 (related to Figure 2): OPC cell numbers do not change between conditions

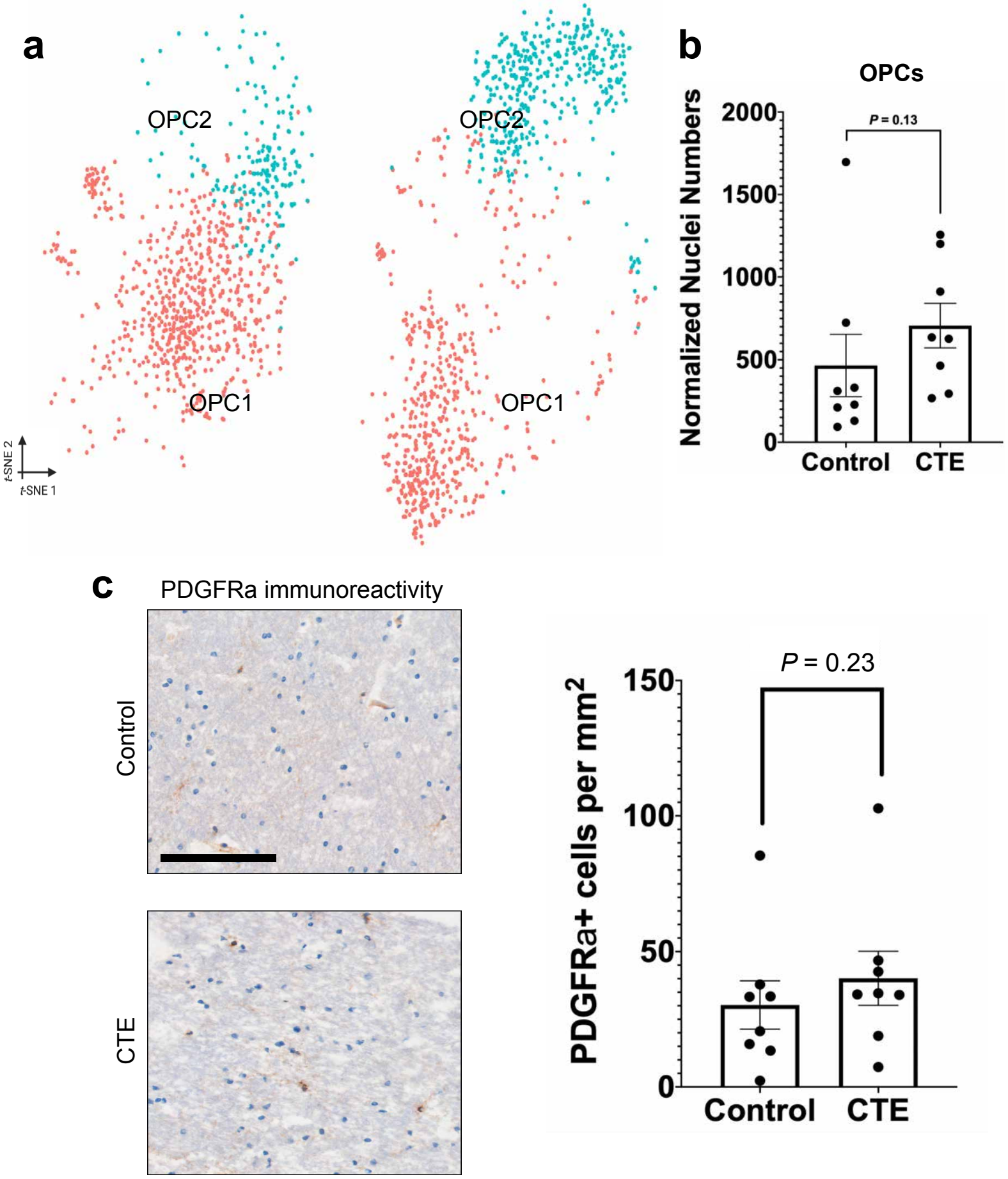

Figure 3. Iron accumulation in CTE-specific oligodendrocytes

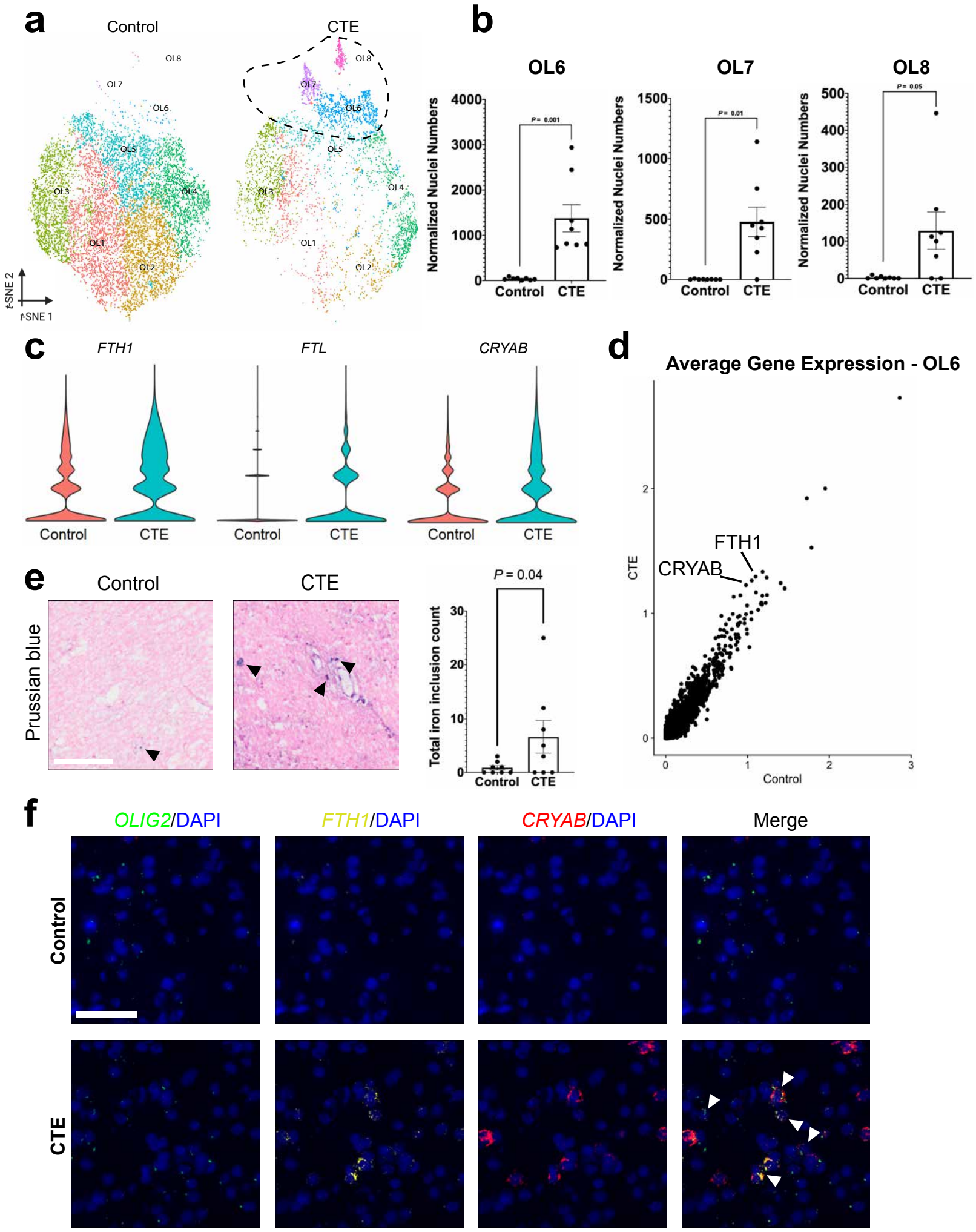

Supplementary Figure 5 (related to Figure 3): Validation of iron accumulation in CTE-specific oligodendrocytes

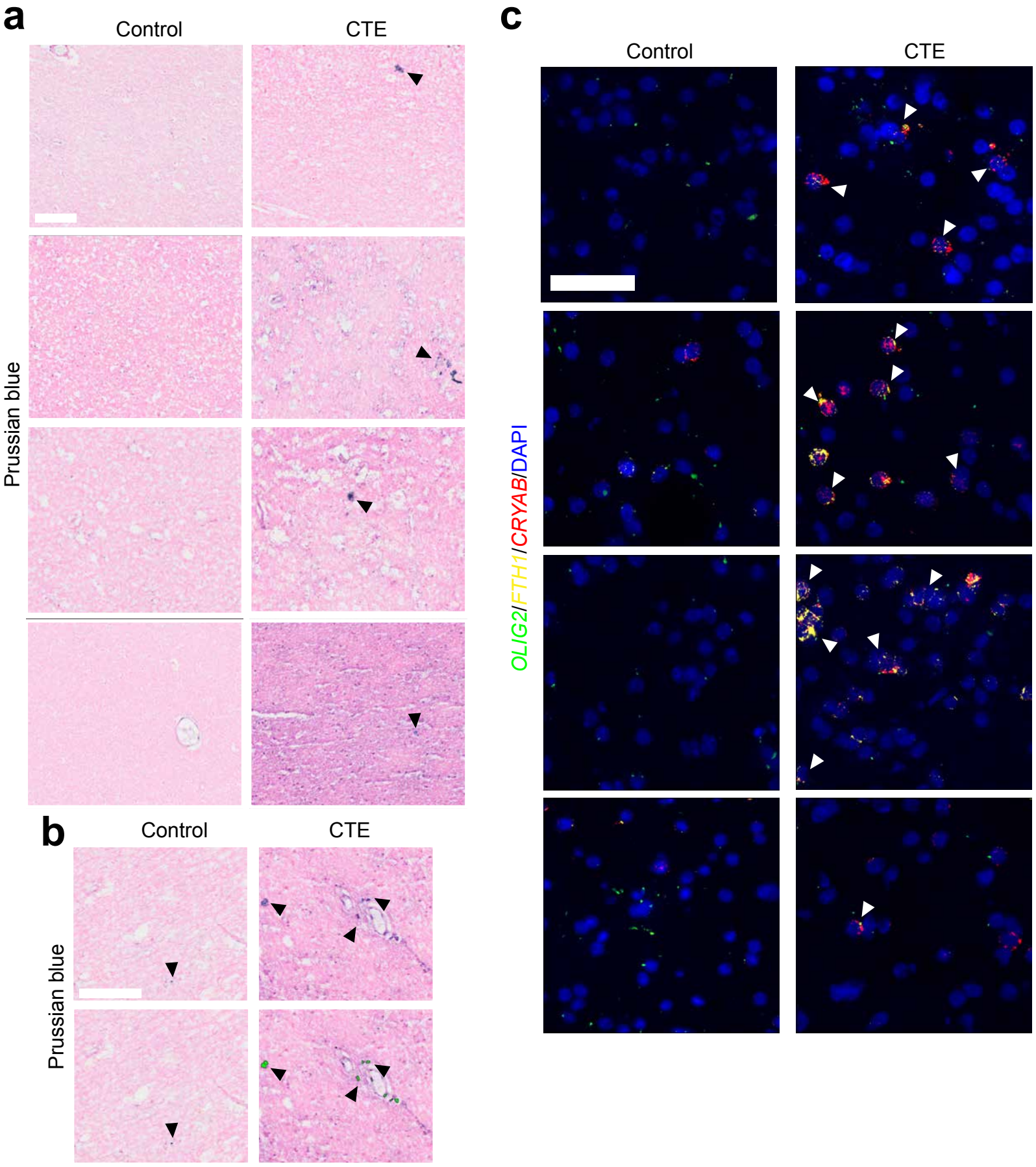

Figure 4. Neuroinflammatory astrocytes in CTE white matter.

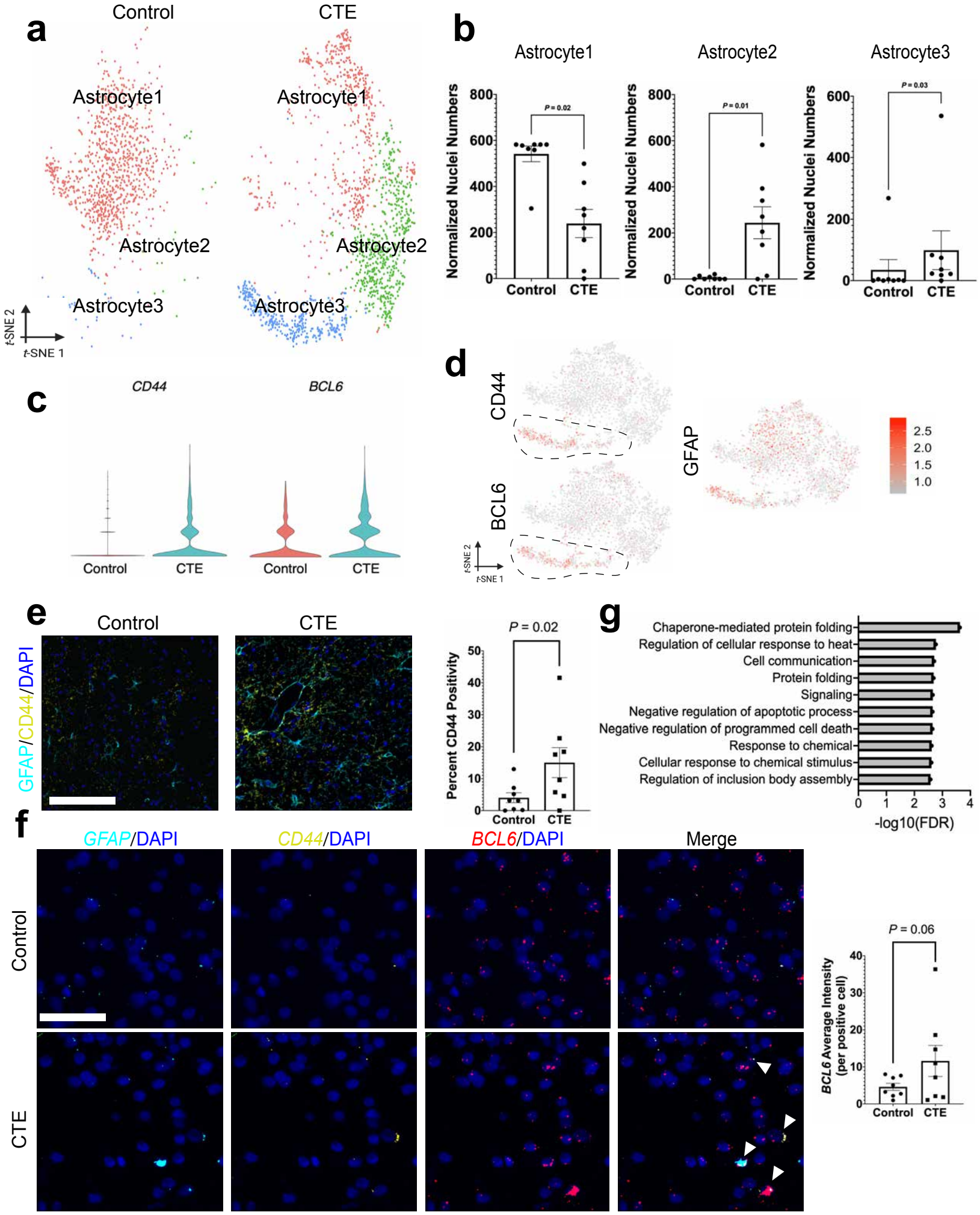

Supplementary Figure 6 (related to Figure 4): Astrocyte cell numbers do not change between conditions

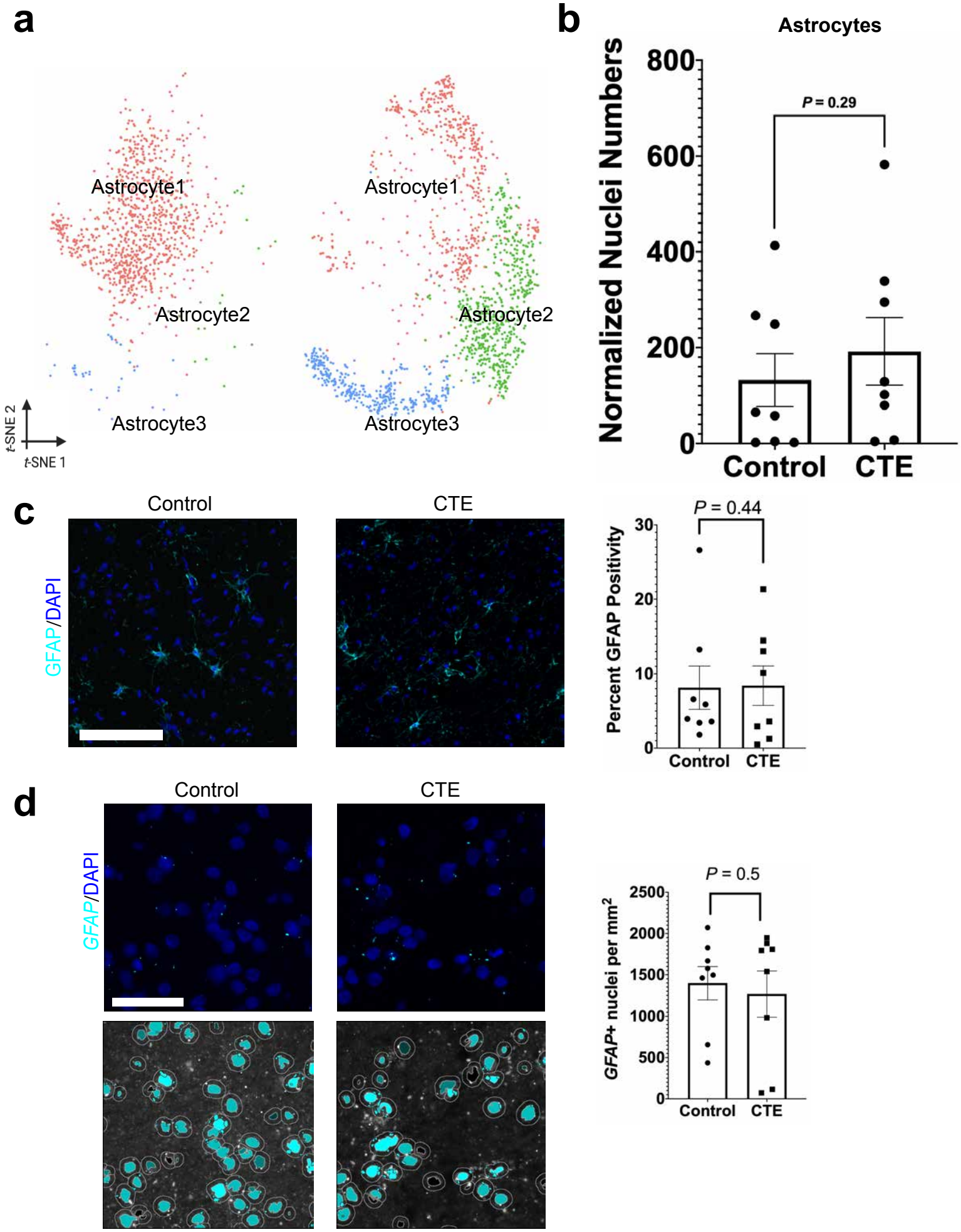
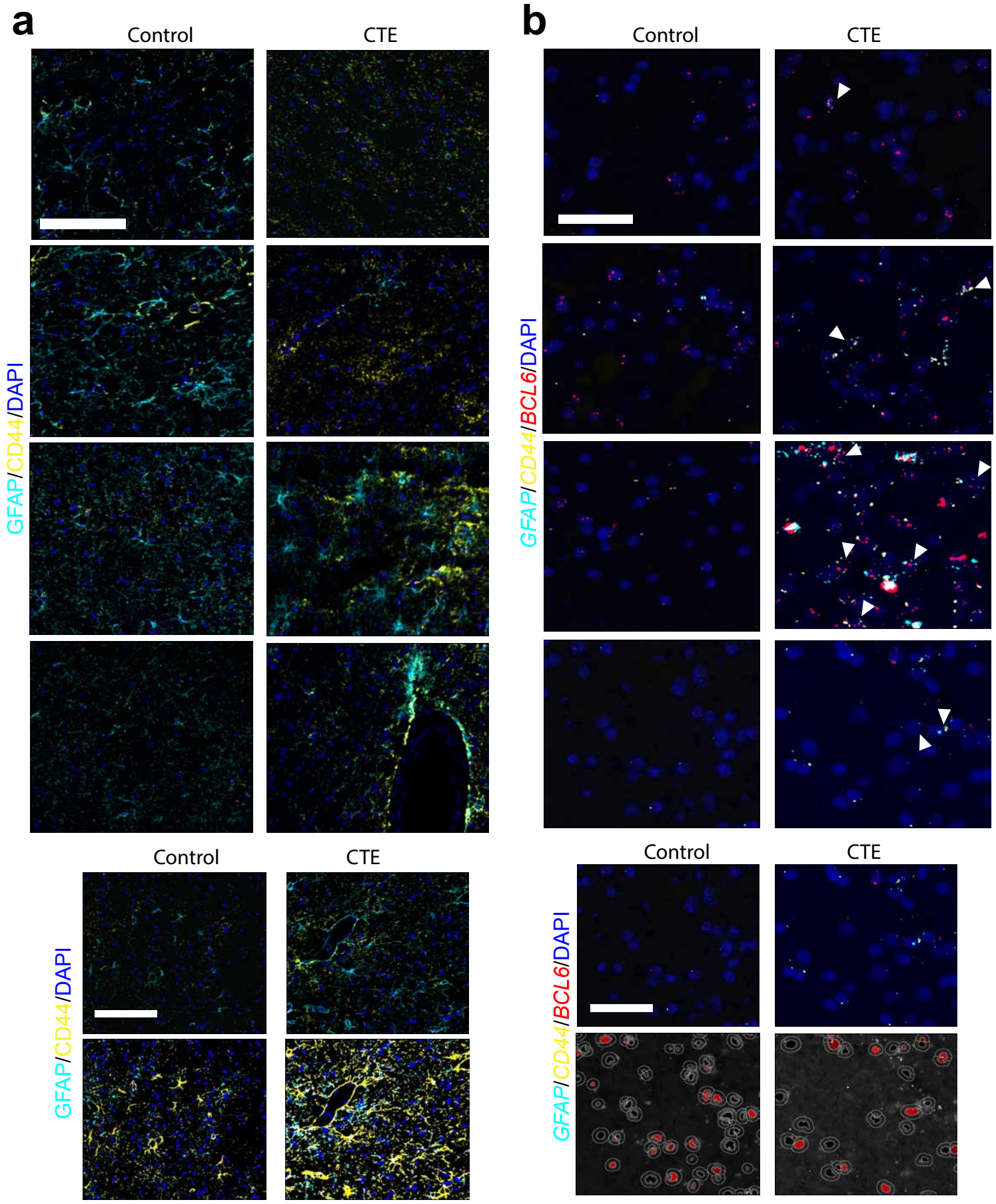
Supplementary Figure 7 (related to Figure 4): Validation of neuroinflammatory astrocytes in CTE white matter